Electronic Supplementary Material (ESI) for Dalton Transactions.

SUPPLEMENTARY INFORMATION

Unveiling the structural transformations of the $PW_{11}Co$@ZIF-67 nanocomposite induced by thermal treatment

Víctor K. Abdelkader-Fernández,[a,*] Diana M. Fernandes,[b,*]

Salete S. Balula,[b] Luís Cunha-Silva,[b,*] Manuel J. Pérez-Mendoza,[a] and Cristina Freire[b]

[a] Departamento de Química Inorgánica, Facultad de Ciencias, Universidad de Granada, Granada, 18071, Spain.

[b] REQUIMTE/LAQV, Departamento de Química e Bioquímica, Faculdade de Ciências da Universidade de Porto, Rua do Campo Alegre, 4169-007 Porto, Portugal.

1. EXPERIMENTAL DETAILS

1.1. Preparation of $PW_{11}Co$@ZIF-67 and derivatives

Reagents and solvents. Cobalt nitrate hexahydrate ($Co(NO_3)_2 \cdot 6H_2O$, ACS reagent, ≥98%, Sigma-Aldrich) and 2-methylimidazole – 2-MeIm – ($C_4H_6N_2$, 99%, Sigma-Aldrich) were employed as received to the synthesis of $PW_{11}Co$@ZIF-67. Methanol (CH_3OH, analytical reagent grade, ≥99.9%, Fisher Scientific) and ultrapure water were used as solvents.

$K_5PW_{11}Co(H_2O)O_{39} \cdot nH_2O$ (abbreviated as $PW_{11}Co$) preparation. The POM was prepared by a previously published procedure.[1] Briefly, an aqueous solution of $K_7PW_{11}O_{39} \cdot nH_2O$ (9.95 g) in 65 mL was heated to 90 ºC and an aqueous solution of metal (3.7 mmol) was added slowly and left under stirring for 15 minutes. The mixture was filtered and cooled down in an ice-bath. A methanol/ethanol (1:1) solution with double volume of the mixture was added and immediately a precipitate is formed. The resultant solid is filtered and dried.

Tubular furnace. The thermal treatments of $PW_{11}Co$@ZIF-67 were carried out in a tubular oven Nabertherm with thermocouple type N and quartz tube, where the precursor was placed on a ceramic boat.

1.2. Physicochemical characterization of $PW_{11}Co$@ZIF-67 and derivatives

Inductively coupled plasma – optical emission spectrometry (ICP-OES) analyses were registered with a spectrometer Optima 4300 DV (Perkin Elmer) with plasma source (RF generator of 40 Hz), and automatic sampler (PerkinElmer AS93-plus). ICP-OES analyses were performed at "*Centro de Apoyo Científico-Tecnológico (CACTUS) de la Universidad de Santiago de Compostela, USC (Galicia, Spain)*".

CHNS analysis were performed with an Elemental Analyzer (TruSpec CHNS model, Leco) equipped with selective and independent IR detectors for carbon, hydrogen and nitrogen, and a differential thermal conductivity detector (TCD) for sulfur quantification. These analyses also were carried out at "*Centro de Apoyo Científico-Tecnológico (CACTUS) de la Universidad de Santiago de Compostela, USC (Galicia, Spain)*".

X-ray photoelectron spectroscopy (XPS) spectra were recorded at "*Centro de Instrumentación Científica de la Universidad de Granada, CIC (Granada, Spain)"*, on a Kratos Axis Ultra-DLD spectrometer equipped with Al/Mg twin anode. Monochromatic Kα radiation in the constant-analyzer-energy mode with pass energies of 160 and 20 eV for the survey and high-resolution spectra was used. Measurements were carried out by carefully extending samples —in form of

finely-divided powder (see the following figure)— on carbon tape supports. Then, analysis zones were selected in regions completely covered by powder, fact that together with the superficial nature of the technique —XPS only collects information from the first few nanometers of the studied material — avoids any contribution from the carbon tape support.

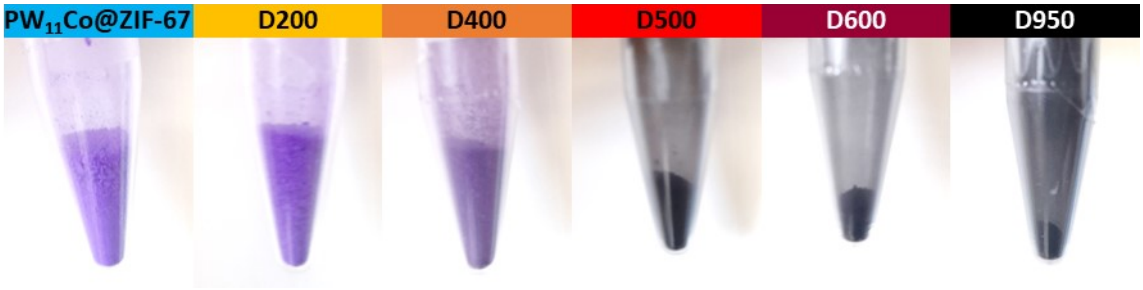

XPS data treatment was performed by using the CasaXPS software (version 2.3.24PR1.0, Casa Software Ltd.). The C 1s transition at 284.6 eV was used as an internal reference. Surface atomic concentrations for the different elements were obtained from the corresponding peak areas (in XPS spectra) and using the relative sensitivity factors (RSF) provided by the manufacturer. The high-resolution XPS spectra were deconvoluted via Levenberg–Marquardt algorithm, i.e., non-linear least squares curve fitting.

Attenuated total reflection Fourier Transform infrared (ATR-FTIR) spectra were recorded on a Jasco FT/IR-460 Plus spectrophotometer in the range 400 – 4000 cm^{-1}, using a resolution of 4 cm^{-1} and 64 scans.

Powder X-ray diffraction (PXRD) patterns were obtained with a Bruker D2 PHASER Diffractometer, involving an X-ray source CuKα (λ = 1.5418 Å; acceleration potential = 45 kV; current = 200 mA). A Bragg-Brentano geometry was used.

The micro-Raman analysis was conducted in the backscattering configuration on a Jobin Yvon HR800 instrument, using a 600 lines/mm grating and the 532 nm laser line from a Nd:YAG DPSS laser (Ventus, Laser Quantum). The spectrometer was operated in the confocal mode, setting the iris to 300 µm. The analysis were conducted at Centro de Investigação em Materiais Cerâmicos e Compósitos – CICECO – University of Aveiro (Aveiro, Portugal). Raman spectra were deconvoluted into 2 and 5 components with MagicPlot Pro software (2.7.2 version).

Gas adsorption/desorption isotherms were recorded by using a Micromeritics' in ASAP 2020 equipment. The N_2 and CO_2 analyses were performed at 77 and 273 K, respectively. Previously, the samples were degassed for 6 hours, under vacuum at 150 °C.

Transmission electronic microscopy (TEM) images were captured with a high-resolution TEM (Hitachi, H9000 NAR), equipped with thermionic emission electron cannon and CCD camera, at

Centro de Investigação em Materiais Cerâmicos e Compósitos – CICECO – University of Aveiro (Aveiro, Portugal). TEM/EDS element distribution maps were acquired by using a JEM-2200FS Field Emission Electron Microscope (JEOL) equipped with a 200 kV field emission gun (FEG) and in-column energy filter (Omega filter).

1.3. Electrochemical characterization of $PW_{11}Co$@ZIF-67 and derivatives

Experimental setup. NOVA software (v2.0) controlled Autolab equipment consisting of a PGSTAT 302 N potentiostat/galvanostat station (EcoChimie B.V.) and a rotating disk electrode (RDE) (Metrohm AG, Switzerland) was used for the electrochemical tests. The measurements were performed with a 3-electrode cell setup where the working electrode was a glassy carbon disk electrode (ø = 3 mm, Metrohm) upon which the sample ink was previously deposited. A carbon rod (ø = 2 mm, Metrohm) was used as counter electrode. Applied potentials were registered against an Ag/AgCl reference electrode (3 mol dm^{-3} $KCl_{(aq)}$, Metrohm ($E_{Ag/AgCl}$)) and converted to reversible hydrogen electrode potentials (E_{RHE}) using the Nernst equation: $E_{RHE} = E_{Ag/AgCl} + 0.059pH + E°_{Ag/AgCl}$ (with $E°_{Ag/AgCl}$ = 0.197 V at 25 °C).

Preparation of sample-modified working electrodes (WE). Prior to sample ink dropping, the glassy carbon disk was conditioned via polishing with three different particle size diamond pastes (6, 3 and 1 mm, MetaDi®ll, Buehler) and alumina powder (0.3 mm, MicroPolish Alumina, Buehler), and thoroughly rinsed with ultrapure water (ρ = 18.2 MU cm, Millipore). To prepare a homogeneous sample dispersion, 1.0 mg of the studied material was mixed with 20 mL of Nafion® 117 solution (Sigma-Aldrich) and 250 mL of N,N-dimethylformamide (anhydrous 99.5%, Sigma-Aldrich), and sonicated during 30 min. Lastly, 7.5 mL of the as-prepared electrocatalyst ink was dropped onto the glassy carbon disk (RDE) surface and dried with air flux.

Assessment of electrochemically active surface areas (ECSA). ECSA values exhibited by electrocatalysts are usually calculated by using the equation:

$$ECSA = C_{dl} / C_{ref}$$

where C_{dl} stands for the double-layer capacitance and C_{ref} for the reference capacitance value per unit area. Usually, due to the impossibility of knowing the exact C_{ref} value for specific and structurally complex materials, the majority of reported studies based their *ECSA* evaluations on a straight comparison of the corresponding C_{dl} values, assuming that C_{ref} for all the studied materials are similar, i.e., ranging in the same order of magnitude. However, the different structures and compositions of the samples considered in this work does not allow assume their corresponding reference capacitances are comparable. This fact makes mandatory the

calculation of these C_{ref} values, although they will necessarily be mere approximations, in order to perform a more reliable comparison of the electrochemically active surface areas.

- Calculation of double-layer capacitances (C_{dl}):

C_{dl} values were calculated via standard double-layer charging test, namely, acquisition of consecutive CV plots at different scan rates (from 20 to 160 $mV \cdot s^{-1}$), being the double-layer capacitance estimated from the slope of linear-fitted plot of current density at 0.8 V *vs.* RHE - $j_{0.8}$ – (non-faradaic region) versus the scan rate (k):

$$j_{0.8} = C_{dl} \cdot k$$

Note that the CV plots of the D500 and D600 samples show elevated noise levels due to their very low current intensities, making impossible the calculation of reliable values for their corresponding C_{dl}. See CV plots in **Fig. S3**, and intensity vs. scan rate plots in **Fig. S4**.

- Calculation of 'estimative' reference capacitances (C_{ref}):

Firstly, specific capacitance values for all the materials were calculated from the corresponding CV data and by using the formula:

$$C = Q / (2 \cdot V \cdot m)$$

where C stands for specific capacitance (expressed in F g^{-1}), Q for the charge (in A s), V for the potential range (in V), and m for the mass of sample deposited on the electrode surface (in g). At the same time Q values were obtained by the equation:

$$Q = A / k$$

where A corresponds to the area under the curve of the CV plot (expressed in A V), and k to the scan rate (in V s^{-1}). Then, these calculated C values were referred to the specific area of the material to find their corresponding reference capacitances, C_{ref}, expressed in F m^{-2}. For these calculations, BET surface areas (m^2 g^{-1}) were obtained from the corresponding N_2-adsorption isotherms of ZIF-67 and POM@ZIF-67 nanocomposites.

In all these calculations several error sources contribute to the global uncertainty of the reference capacitances and, consequently, to the finally calculated *ECSA* values. For instance, even if no redox peaks appeared into the CV plots faradaic contributions could not be completely negligible, increasing the measured CV areas and subsequently, leading to overestimated charges and capacitance values. Since the magnitude of faradaic contributions is influenced by a plethora of experimental factors (electrolyte composition, temperature, pH, scan rate, etc.), slight variations in some of these conditions can result in significant changes in the calculated C_{ref} values. Moreover, the use of BET surface values (depending on the N_2 molecules accessibility) in the calculations of electrochemically active surface areas (depending on the

accessibility of the electrolyte) entails the assumption that these two types of area values are comparable. Taking in account these considerations, the *ECSA* values calculated in this work are estimative, but regarding the scope of the study provides the enough accuracy to be used for comparative purposes.

2. OCCUPANCY CALCULATION

The calculation of the occupancy degree the 'in situ'-prepared $PW_{11}Co$@ZIF-67 nanocomposite—expressed as POM units per 100 ZIF cages—is based on:

i. amounts of POM units detected into the nanocomposite (POM unit per gram of nanocomposite) calculated from the W content measured by ICP-OES analysis;

ii. mass of ZIF-67 in this nanocomposite calculated by subtracting the mass of POM to the total nanocomposite mass;

iii. each ZIF-67 cage (unit cell) is formed by 24 Co nodes. However, since all the cobalt nodes are shared by two adjacent cages, the effective number of Co nodes per ZIF-67 cage is 12. Thereupon, the number of ZIF-67 cages per gram of nanocomposite can be calculated from the mass of ZIF-67 in the nanocomposite by using their molar mass—$Co(C_8H_{10}N_4)$, 221.12 g mol^{-1}—the stoichiometric relation of Co nodes per mole of ZIF-67 (1:1) and the known value of 12 metal nodes per unit cell;

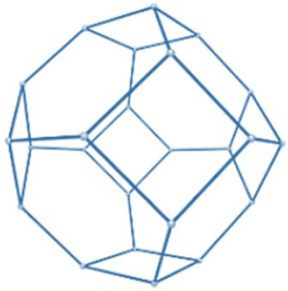

Schematic representation of ZIF-67-unit cell structure (truncated octahedron), where metallic node positions / vertices are marked with red dots.

iv. Finally, when the amount of POM units and ZIF-67-cages present in $PW_{11}Co$@ZIF-67 have been found, the Occupancy degree can be calculated directly:

$$\textit{Occupancy (\%)} = [(\textit{POM units/g nanocomposite}) / (\textit{ZIF-cages/g nanocomposite})] \times 100$$

3. PROBABLE ORIGIN FOR THE LOW W/P RATIOS DETECTED BY XPS OF POM UNITS INDIVIDUALLY CONFINED INTO ZIF-67 CAGES

A plausible explanation for the POM W/P ratio distortion to low values can be given on the basis of (i) the surface nature of XPS analysis and (ii) the 3D complex guest@host nanoarrangement adopted by the $PW_{11}Co$@ZIF-67 nanocomposite. If a major part of the individually encapsulated $PW_{11}Co$ units is located in the limit depth of the XPS detection range a part of W atoms can remain undetected decreasing the W atomic concentration and, consequently the calculated W/P atomic ratio. See the following figure for a tentative graphic description of this phenomenon.

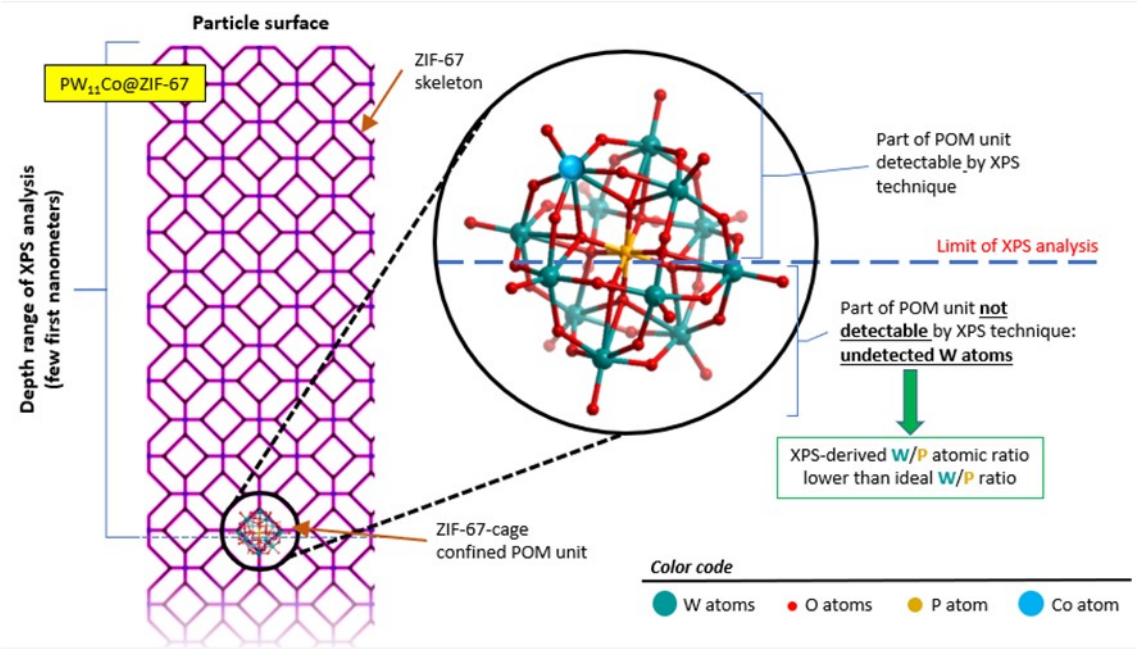

4. TABLES

Table S1. Proposed assignations of chemical moieties/environments for the components obtained by XPS high-resolution spectra curve fitting. Components are labelled as in Tables S3 and S4, and Figure S1.

Element	Component	Assignation	
K 1s	**K1**	K(I)	*from POM salt*
C 1s	**C1**	C(sp^2)	*from nanocarbon* [2-4]
	C2	C-C / C-N	*from ZIF-67 and adventitious carbon* [5-7]
		C(sp^3) / -C-NH-C (pyrrolic) /	*from nanocarbon* [2-4, 8]
	C3	C-O / N-C-N	*from ZIF-67 and adventitious carbon* [5, 6, 9]
		-C-O / -C=N-C (pyridinic)	*from nanocarbon* [2, 3, 8]
	C4	-C=O	*from nanocarbon* [2, 3]
	C5	$-COO^-$ / CO_3^{2-}	*from ZIF-67 and adventitious carbon* [5, 7]
		$-COO^-$	*from nanocarbon* [2, 3]
	C6	Shake-up (ShU)	*from nanocarbon* [10]
	C7	Plasmon	*from nanocarbon* [2, 3]
O 1s	**O1**	O–W	*from POM*
		CoO / WO_3 / WO_2	*from nanocarbon support* [11, 12]
	O2	-C–O	*from adventitious carbon* [5]
		-C=O	*from nanocarbon* [13]
	O3	O–Co / O–P	*from POM*
	O4	$-COO^-$ / CO_3^{2-} / NO_3^-	*from adventitious carbon and ZIF-67* [5, 14]
		-C–O	*from nanocarbon* [13]
	O5	-OH / H_2O --- Co	*from ZIF-67* [7]
	O6	$-COO^-$ / H2O	*from nanocarbon* [13]
N 1s	**N1**	N–$©_2$	*from ZIF-67* [6, 7, 9]
		-C=N-C (pyridinic)	*from nanocarbon* [8]
	N2	N–H / NH_4^+	*from ZIF-67* [7, 15]
		-C-NH-C (pyrrolic)	*from nanocarbon* [8]
	N3	Quaternary N	*from nanocarbon* [8]
	N4	O=N-C	*from nanocarbon* [8]
	N5	NO_3^-	*from ZIF-67* [16]
Co 2p	**Co1**	Co^0	*from nanocarbon* [11]
	Co2	Co(II)	*from POM and ZIF-67* [17]
		CoO	*from nanocarbon* [11]
	Co3	Co-C interaction	*from nanocarbon* [11]
	Co4	Satellite	*from POM, ZIF-67 and nanocarbon* [11]

P 2p	**P1**	Metal phosphide	*from nanocarbon* [18]
	P2	P-O	*from POM*
W 4f	**W1**	W^0	*from nanocarbon* [5]
	W2	W−O	*from POM*
	W3	Loss feature	*from POM and nanocarbon*

Table S2. Core-level binding energies (BE) and FWHM values of the components for the "pure" ZIF-67, the $PW_{11}Co$@ZIF-67 precursor, and the derived nanocomposites, obtained by curve fitting (deconvolution) of XPS spectra.

Sample	Element	BE (eV)[1] Component 1	2	3	4	5	6	7
$PW_{11}Co$ ("pure" POM)	K 2p[2]	293.3 (1.28)						
	C 1s		284.8 (1.32)	286.5 (1.32)		289.1 (1.32)		
	O 1s	530.8 (1.24)	532.1 (1.24)	532.7 (1.24)	532.8 (1.24)		533.8 (1.24)	
	Co 2p[3]		781.3 (2.55)		785.3 (6.82)			
	P 2p[4]		134.3 (1.15)					
	W 4f[5]		35.9 (1.01)	41.7 (2.24)				
ZIF-67 ("pure" MOF)	C 1s		284.9 (1.36)	286.1 (1.36)		288.4 (1.36)		
	O 1s		531.6 (1.72)	532.6 (1.72)		534.1 (1.72)		
	N 1s	399.1 (1.27)	400.7 (1.27)			406.9 (1.27)		
	Co 2p[3]		781.4 (2.47)		786.4 (5.70)			
$PW_{11}Co$@ZIF-67	C 1s		284.8 (1.41)	286.0 (1.41)		288.5 (1.41)		
	O 1s	530.5 (1.62)	531.7 (1.62)	532.8 (1.62)	533.2 (1.62)	534.2 (1.62)		
	N 1s	399.0 (1.34)	400.5 (1.34)			407.3 (1.34)		
	Co 2p[3]		781.2 (2.69)		785.5 (6.80)			
	P 2p[4]		132.1 (1.06)					
	W 4f[5]		35.4 (1.41)	41.0 (3.26)				
D200	C 1s		284.8 (1.41)	286.1 (1.41)		288.5 (1.41)		
	O 1s	530.4 (1.61)	531.6 (1.61)	532.8 (1.61)	533.1 (1.61)	534.2 (1.61)		
	N 1s	398.9	400.5			407.4		

		(1.35)	(1.35)			(1.35)		
	Co 2p[3]		781.1 (2.74)		785.5 (6.48)			
	P 2p[4]		132.0 (1.07)					
	W 4f[5]		35.3 (1.43)	40.4 (5.00)				
D400	C 1s	284.5 (1.44)	284.8 (1.44)	286.3 (1.44)	287.6 (1.44)	288.5 (1.44)	291.1 (2.16)	
	O 1s	530.2 (1.66)	531.8 (1.66)	532.8 (1.66)	533.3 (1.66)	534.2 (1.66)	535.4 (1.66)	
	N 1s	398.9 (1.41)	400.5 (1.41)	401.8 (1.41)		407.2 (1.41)		
	Co 2p[3]		780.9 (2.76)		785.3 (6.42)			
	P 2p[4]		131.2 (2.71)					
	W 4f[5]		35.0 (1.32)	40.0 (5.00)				
D500	C 1s	284.3 (1.41)	284.8 (1.41)	286.1 (1.41)	287.3 (1.41)	288.7 (1.41)	289.8 (2.12)	291.9 (2.12)
	O 1s	530.2 (1.87)	531.6 (1.87)		533.3 (1.87)		535.5 (1.87)	
	N 1s	398.6 (1.61)	400.3 (1.61)	401.8 (1.61)	404.0 (1.61)			
	Co 2p[3]	778.7 (2.27)	780.5 (2.27)	782.2 (2.27)	785.3 (6.96)			
	P 2p[4]	128.7 (1.68)	132.8 (1.68)					
	W 4f[5]		35.0 (1.30)	39.9 (4.93)				
D600	C 1s	284.1 (1.21)	284.8 (1.21)	285.9 (1.21)	286.9 (1.21)	288.5 (1.21)	289.6 (1.82)	
	O 1s	530.1 (1.91)	531.7 (1.91)		533.3 (1.91)		535.5 (1.91)	
	N 1s	398.5 (2.12)	400.2 (2.12)	401.8 (2.12)	404.2 (2.12)			
	Co 2p[3]	779.1 (2.59)	780.4 (2.59)	782.2 (2.59)	785.3 (6.20)			
	P 2p[4]	128.6 (1.84)	133.4 (1.84)					
	W 4f[5]		35.2 (1.52)	38.3 (4.45)				
D950	C 1s	284.1 (1.03)	284.8 (1.03)	285.9 (1.03)	287.0 (1.03)	288.4 (1.03)	289.6 (1.55)	291.7 (1.55)
	O 1s	529.9 (1.79)	531.5 (1.79)		533.2 (1.79)		535.1 (1.79)	
	N 1s	398.4 (2.63)	399.9 (2.63)	401.8 (2.63)	402.8 (2.63)			
	Co 2p[3]	779.1 (2.27)	780.4 (2.27)	782.1 (2.27)	785.3 (7.71)			
	P 2p[4]	129.0 (1.96)	133.4 (1.96)					
	W 4f[5]	31.1	35.2	39.7				

		(0.62)	(1.37)	(4.29)				

[1] The values between brackets refer to the full width at half-maximum (FWHM) of the bands.

[2] Only the 3/2 component is included. BE value for the corresponding ½ component is shifted 2.2 eV (significant spin-orbit coupling splitting).

[3] Only 3/2 components are included. BE values for the corresponding ½ components are shifted 15.7 eV (strong spin-orbit coupling splitting).

[4] Only the 3/2 component is included. BE value for the corresponding ½ component is shifted 0.9 eV (weak spin-orbit coupling splitting).

[5] Only the 7/2 component is included. BE value for the corresponding 5/2 component is shifted 2.2 eV (significant spin-orbit coupling splitting).

Table S3. Relative proportions of the components for the "pure" ZIF-67, the $PW_{11}Co$@ZIF-67 precursor, and the derived nanocomposites, obtained by curve fitting (deconvolution) of XPS spectra.

Sample	Element	Relative abundance (%)						
		Component						
		1	2	3	4	5	6	7
$PW_{11}Co$ ("pure" POM)	K 2p	100.0						
	C 1s		79.2	13.9		6.9		
	O 1s	75.9	14.6	3.1	3.5		2.9	
	Co 2p		42.9		57.1			
	P 2p		100.0					
	W 4f		89.8	10.2				
ZIF-67 ("pure" MOF)	C 1s		71.5	25.0		3.6		
	O 1s		32.9	25.9		41.2		
	N 1s	85.0	10.6			4.4		
	Co 2p		53.2		46.8			
$PW_{11}Co$@ZIF-67	C 1s		74.3	19.4		6.3		
	O 1s	15.4	57.2	0.7	24.5	2.2		
	N 1s	87.8	10.3			2.2		
	Co 2p		43.6		56.4			
	P 2p		100.0					
	W 4f		87.0	13.0				
D200	C 1s		75.3	17.8		6.9		
	O 1s	18.7	53.8	0.9	24.9	1.7		
	N 1s	86.1	11.1			2.8		
	Co 2p		45.0		55.0			
	P 2p		100.0					
	W 4f		81.7	18.3				
D400	C 1s	0.7	72.3	17.0	1.0	9.0	0.1	
	O 1s	12.4	49.6	0.6	31.1	2.7	3.7	
	N 1s	77.4	14.4	5.9		2.4		
	Co 2p		44.8		55.2			
	P 2p		100.0					
	W 4f		76.3	23.7				
D500	C 1s	15.5	53.3	14.7	5.8	7.0	3.1	0.7
	O 1s	28.7	47.1		22.7		1.5	
	N 1s	68.6	19.9	7.3	4.3			

	Co 2p	3.1	31.0	13.8	52.1			
	P 2p	4.4	95.6					
	W 4f		78.0	22.0				
D600	C 1s	25.9	40.0	17.0	6.6	6.9	3.7	
	O 1s	30.9	40.7		27.0		1.4	
	N 1s	56.5	24.5	10.9	8.1			
	Co 2p	6.2	30.3	13.6	49.9			
	P 2p	5.4	94.6					
	W 4f		62.1	37.9				
D950	C 1s	61.2	18.6	7.9	3.7	3.7	3.7	1.2
	O 1s	42.4	34.1		21.1		2.5	
	N 1s	41.4	37.3	17.8	3.5			
	Co 2p	16.7	24.3	11.8	47.2			
	P 2p	17.0	83.0					
	W 4f	7.6	74.9	17.5				

Table S4. Intensity and FWHM values for the D and G bands in 2-component deconvolutions of D500, D600, and D950 Raman spectra.

Sample	D band		G band	
	Intensity	FWHM (cm^{-1})	Intensity	FWHM (cm^{-1})
D500	69.5	221.6	56.9	99.2
D600	19.0	131.3	17.1	82.1
D950	50.9	113.6	48.2	72.9

Table S5. Position and FWHM values for the D4, D, D3, G, and D' bands in 5-component deconvolutions of D500, D600, and D950 Raman spectra.

sample	Position (cm^{-1})					FWHM (cm^{-1})				
	D4	D	D3	G	D'	D4	D	D3	G	D'
D500	1208.0	1322.2	1450.7	1583.5	1617.8	147.5	119.9	248.8	57.9	48.1
D600	1310.4	1347.2	1494.1	1587.2	1616.1	185.7	102.6	184.6	66.6	22.4
D950	1293.7	1344.2	1503.9	1582.3	1615.1	257.7	89.0	151.3	56.6	30.9

Table S6. Capacitance and electroactive surface area values of the "pure" ZIF-67, the $PW_{11}Co$@ZIF-67 precursor, and their derived nanocomposites.

Sample	Area-related parameter		
	C_{ref}[a] (μF/cm^2)	C_{dl}[b] (μF)	$ECSA$[c] (m^2/g)
ZIF-67	0.017	2.33	490
$PW_{11}Co$@ZIF-67	0.026	3.97	555
D200	0.035	2.29	233
D400	0.008	1.15	490
D500	0.037	-	-
D600	0.034	-	-
D950	16.823	29.30	6

[a]Reference capacitances per unit area. [b]Double-layer capacitance values. [c]Electrochemically active surface areas. For details and calculations see Experimental Section of SI

5. FIGURES

C 1s core-level deconvolutions

$PW_{11}Co$ "pure"

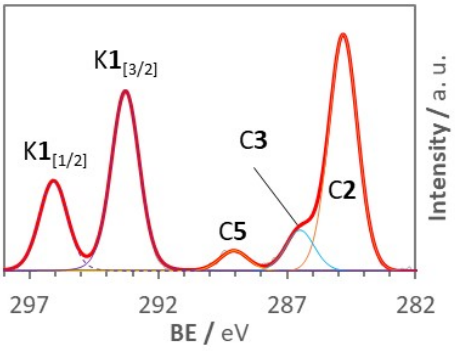

ZIF-67 "pure"

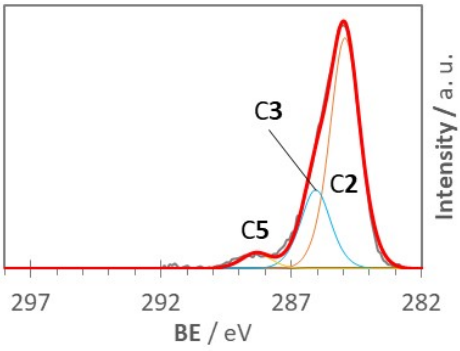

$PW_{11}Co$@ZIF-67

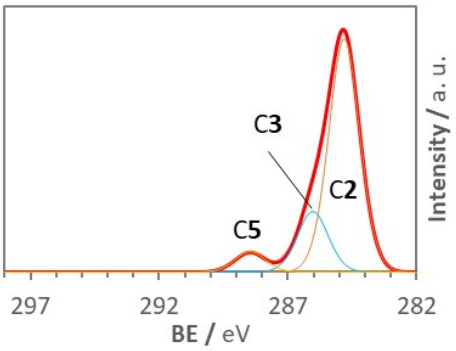

D200

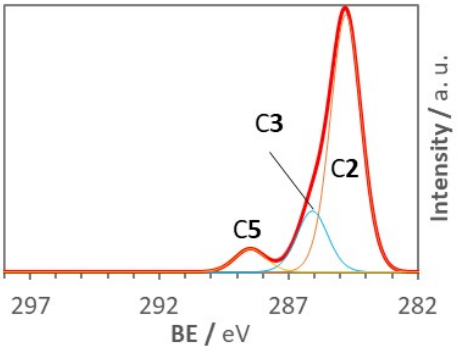

D400

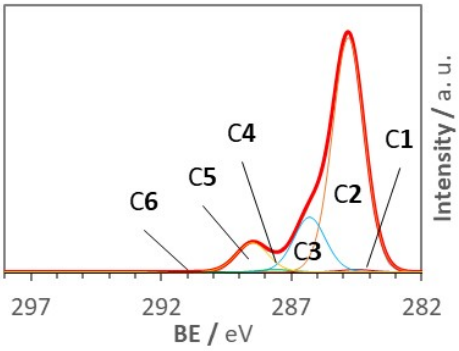

D500

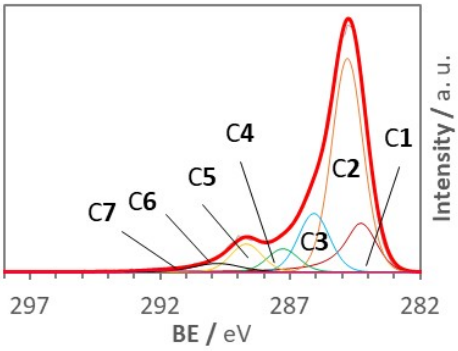

D600

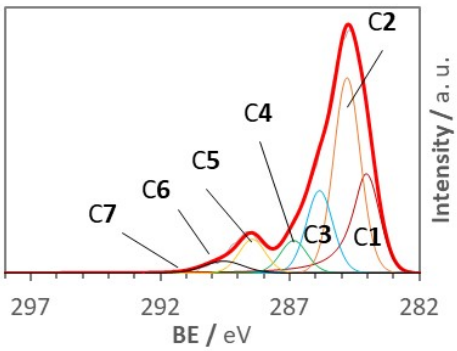

D950

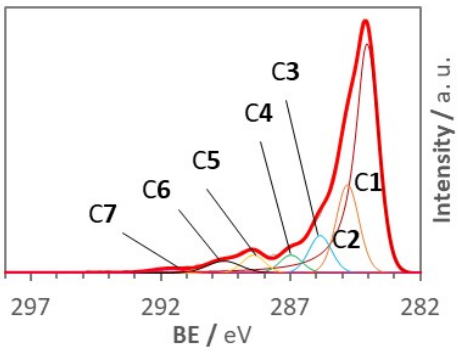

O 1s core-level deconvolutions

$PW_{11}Co$ “pure”

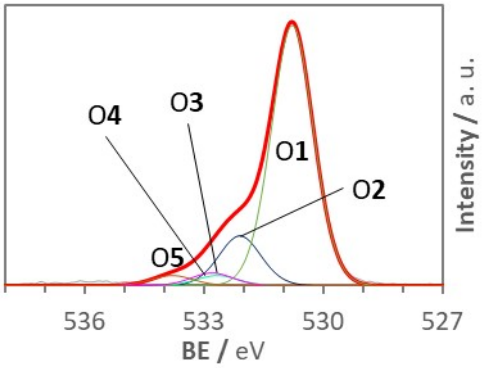

ZIF-67 “pure”

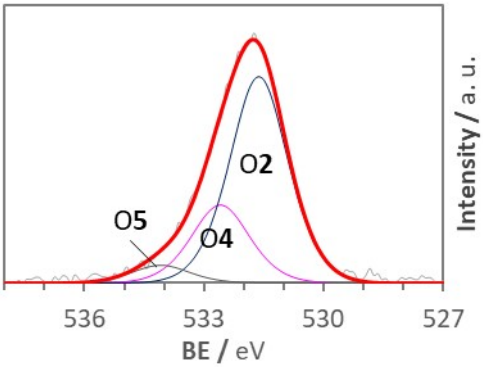

$PW_{11}Co$@ZIF-67

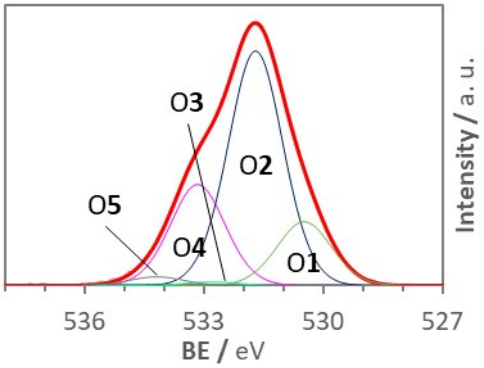

D200

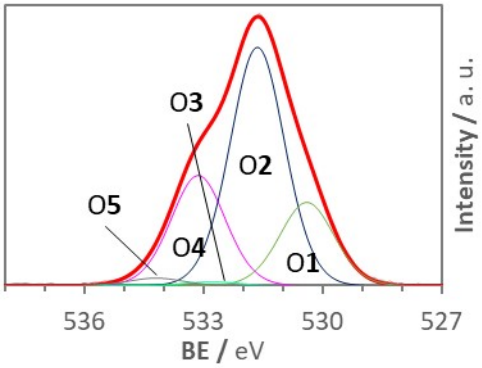

D400

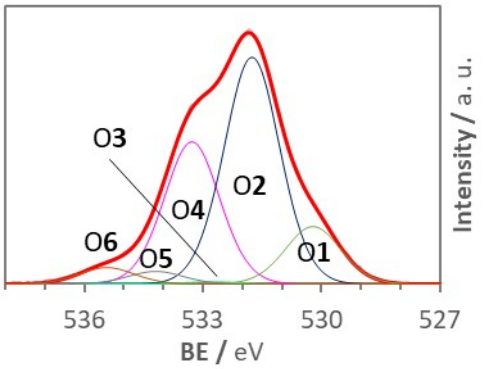

D500

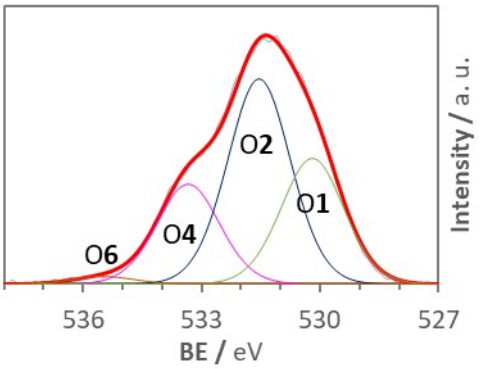

D600

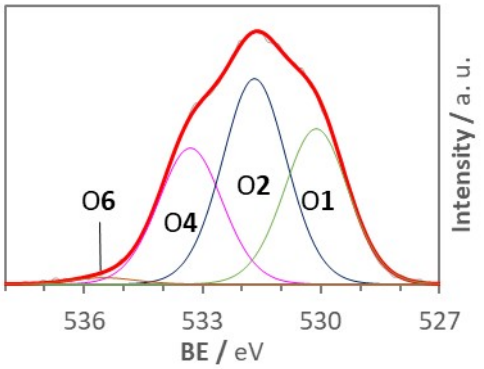

D950

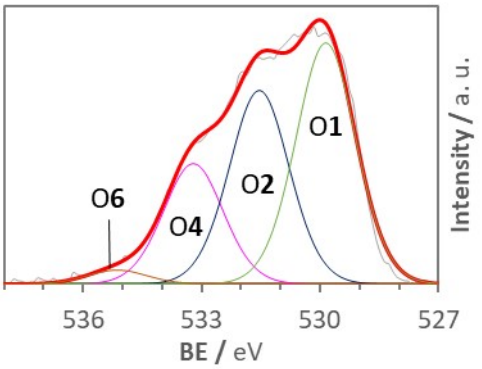

N 1s core-level deconvolutions

$PW_{11}Co$ “pure”

X

ZIF-67 “pure”

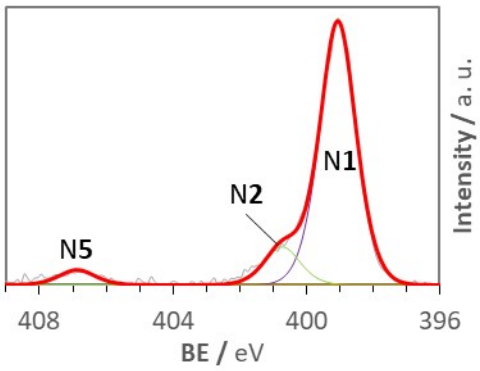

$PW_{11}Co$@ZIF-67

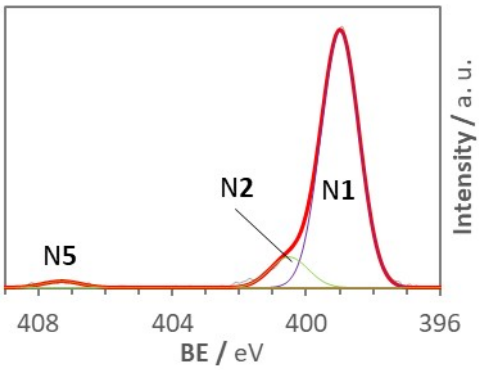

D200

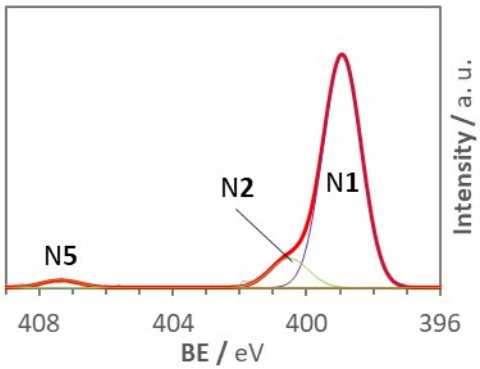

D400

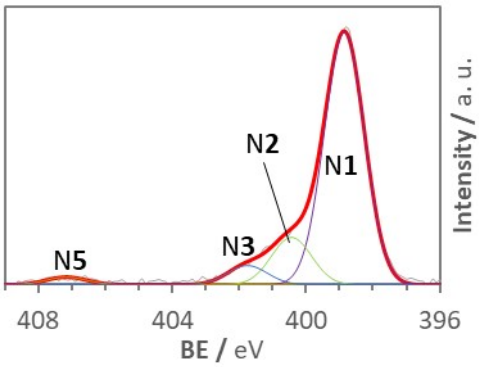

D500

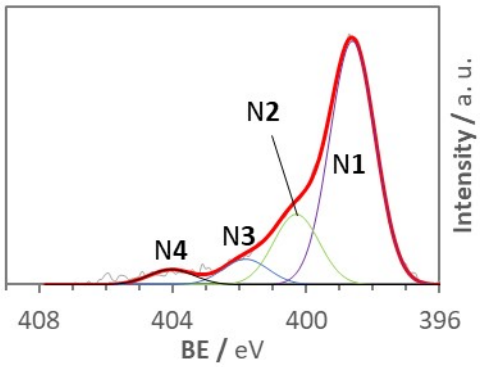

D600

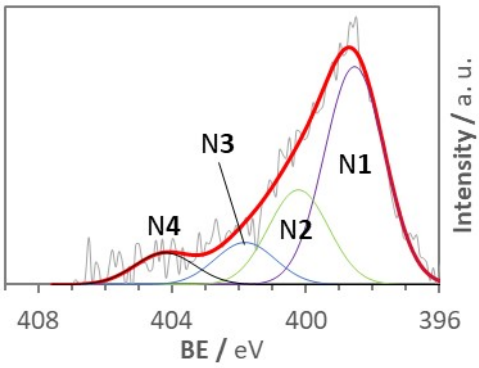

D950

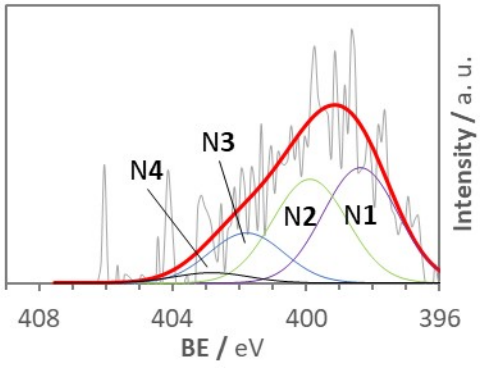

Co 2p core-level deconvolutions (3/2 regions)

$PW_{11}Co$ "pure"

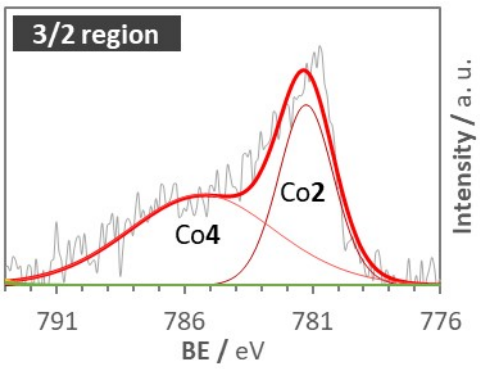

ZIF-67 "pure"

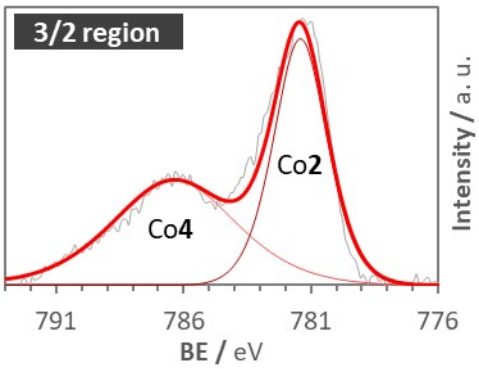

$PW_{11}Co$@ZIF-67

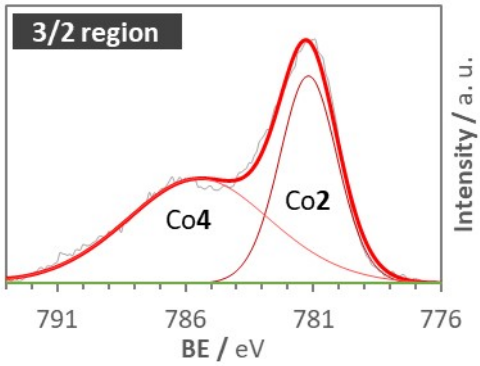

D200

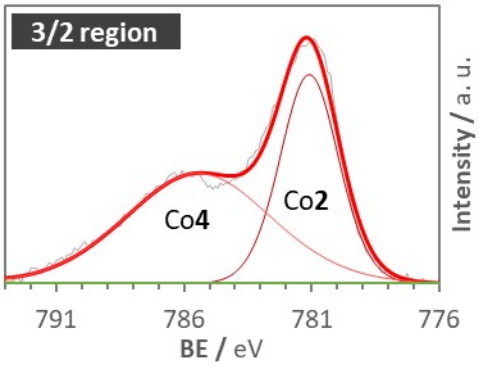

D400

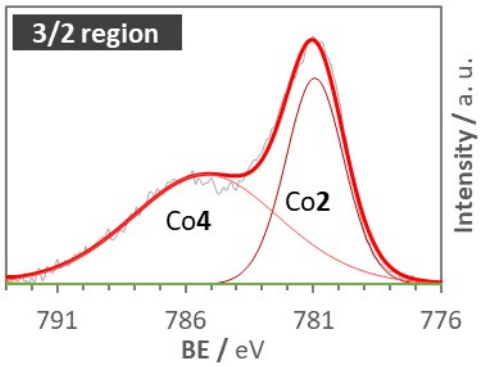

D500

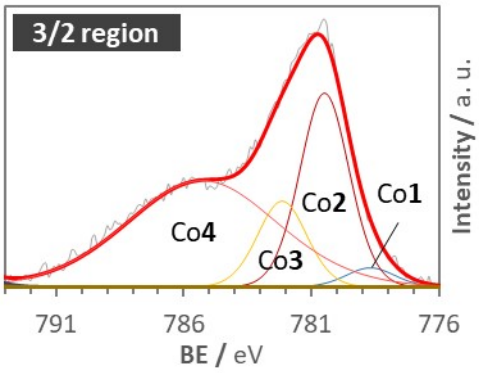

D600

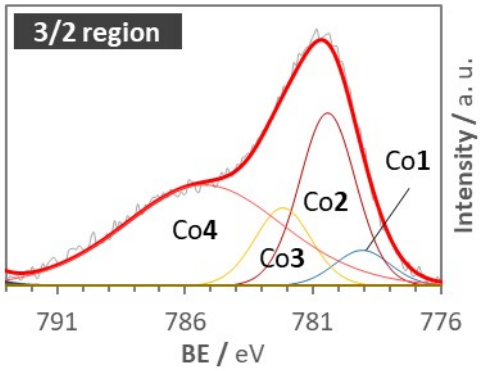

D950

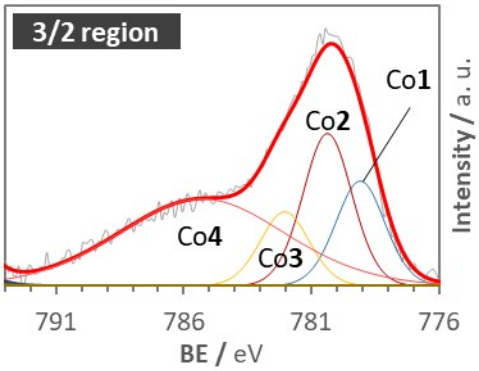

P 2p core-level deconvolutions

$PW_{11}Co$ “pure”

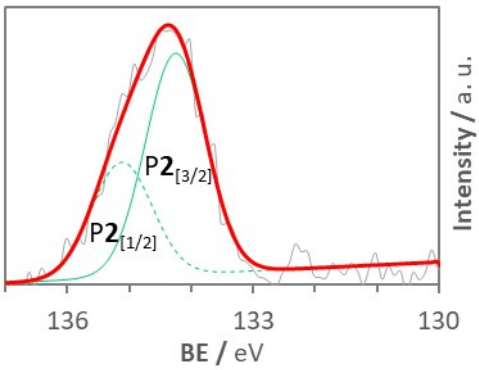

ZIF-67 “pure”

X

$PW_{11}Co$@ZIF-67

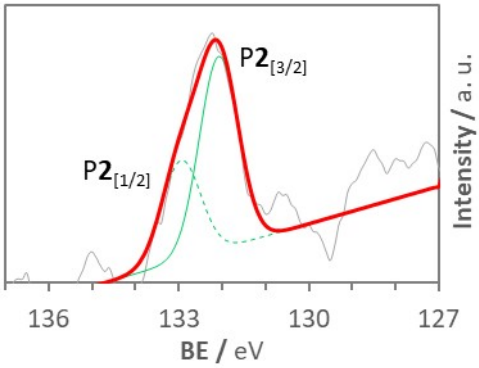

D200

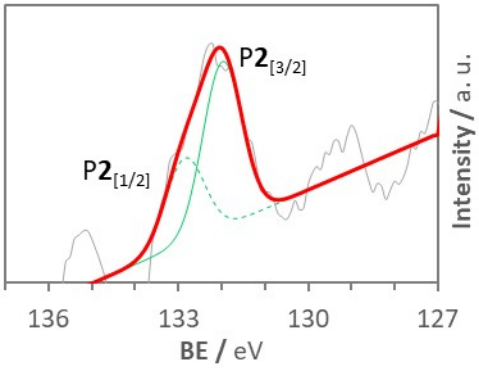

D400

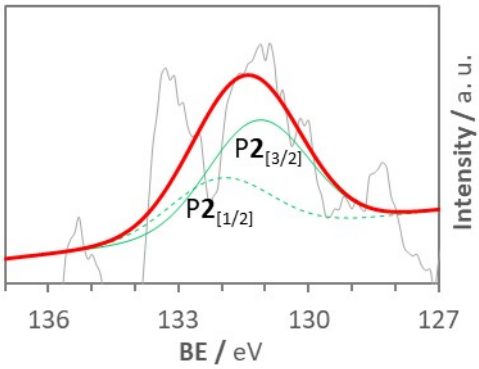

D500

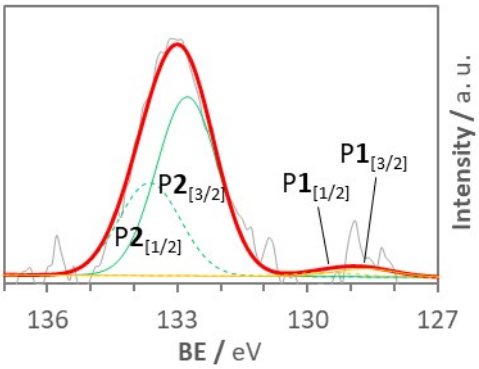

D600

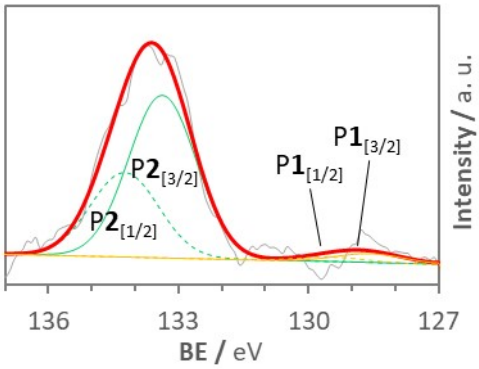

D950

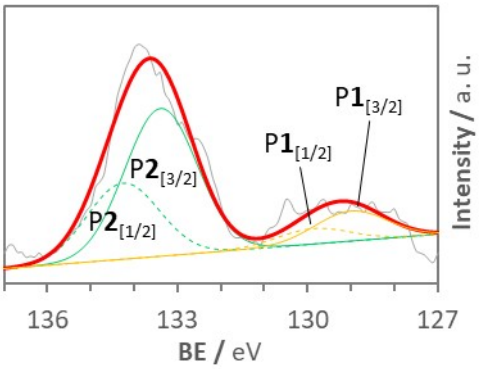

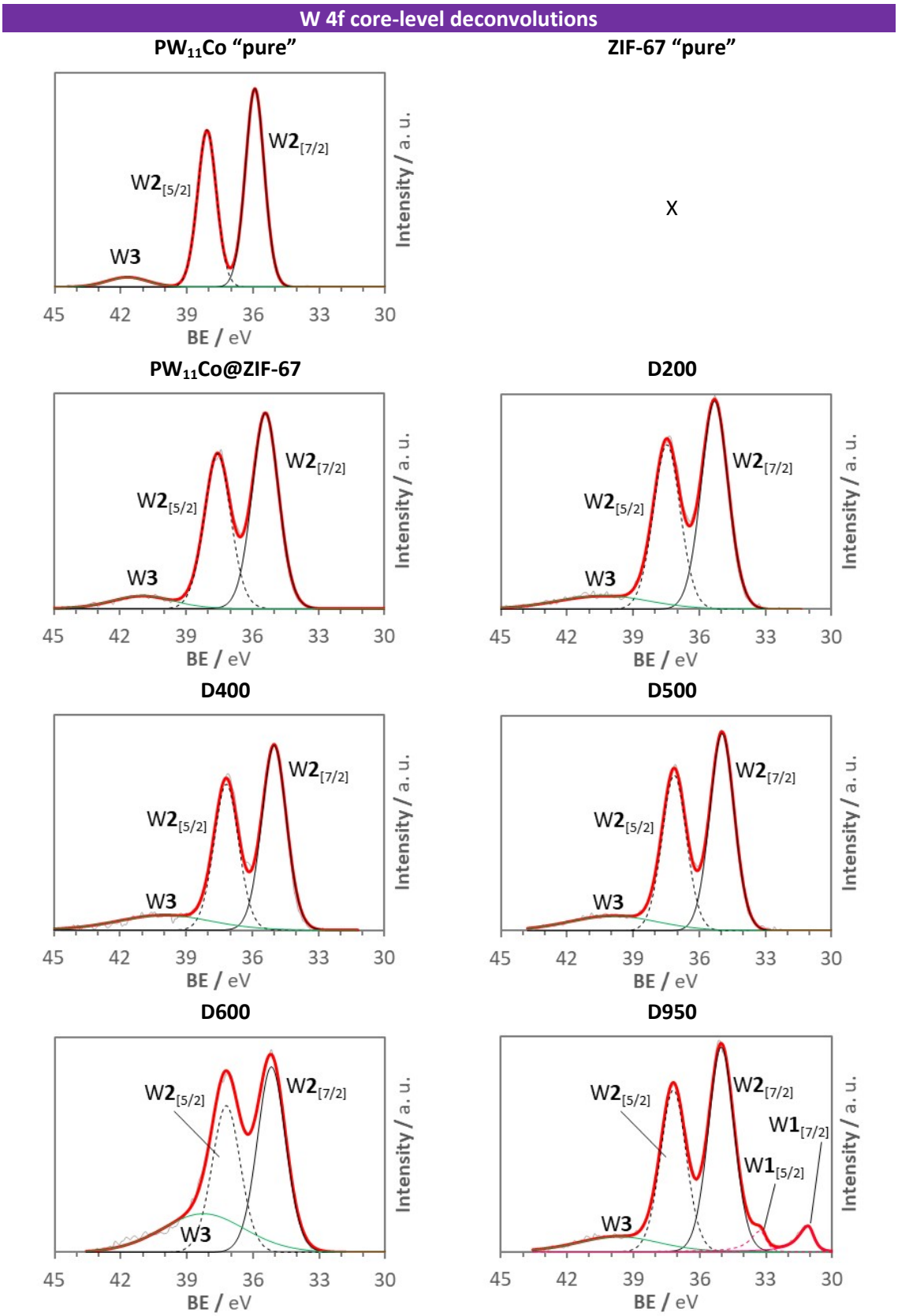

Figure S1. Deconvolutions of XPS high-resolution C 1s, O 1s, N 1s, Co 2p, P 2p, and W 4f core-level regions for the “pure” $PW_{11}Co$ and ZIF-67, the $PW_{11}Co$@ZIF-67 precursor, and the derived nanocomposites. *In the case of Co 2p, only 3/2 regions were included for clarity.*

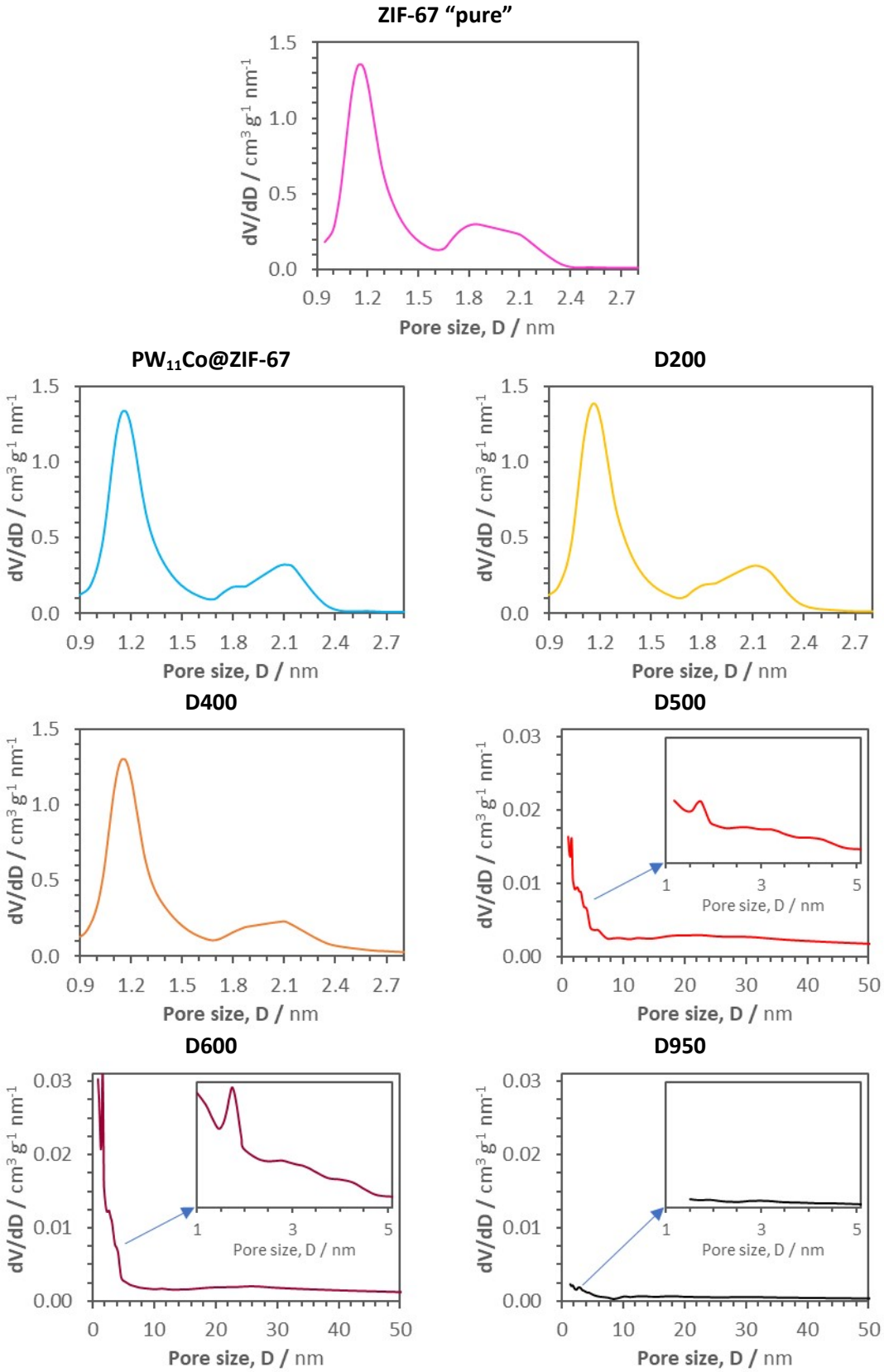

Figure S2. Pore size distributions of the “pure” ZIF-67, the $PW_{11}Co$@ZIF-67 precursor, and the derived nanocomposites, obtained via Horvath-Kawazoe method from the corresponding N_2-adsorption isotherm data.

ZIF-67 “pristine”

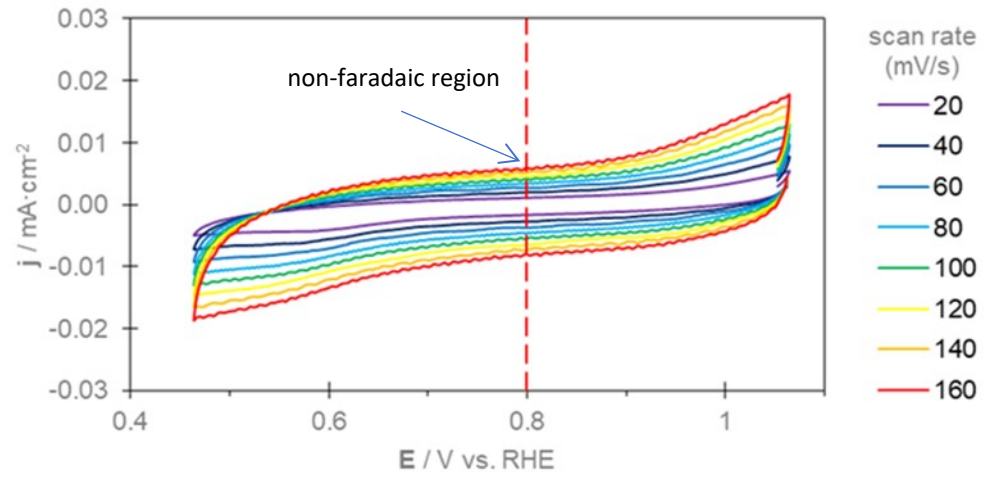

$PW_{11}Co$@ZIF-67

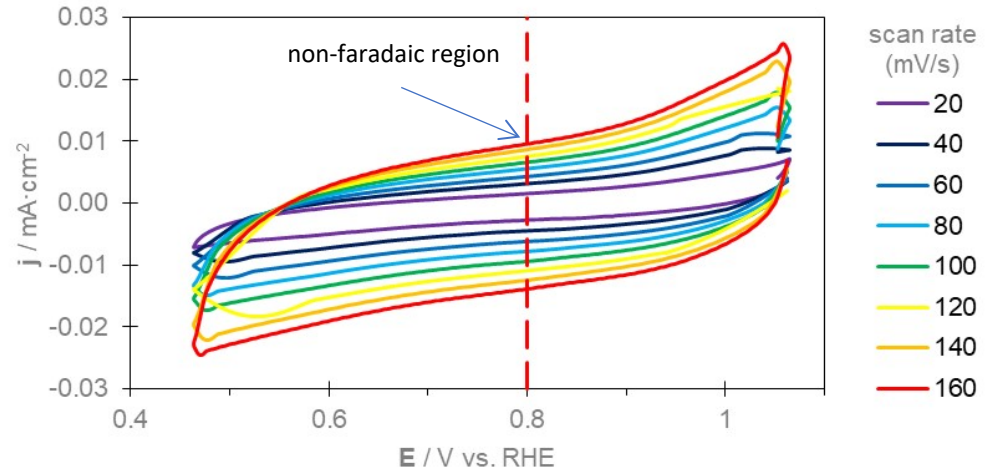

D200

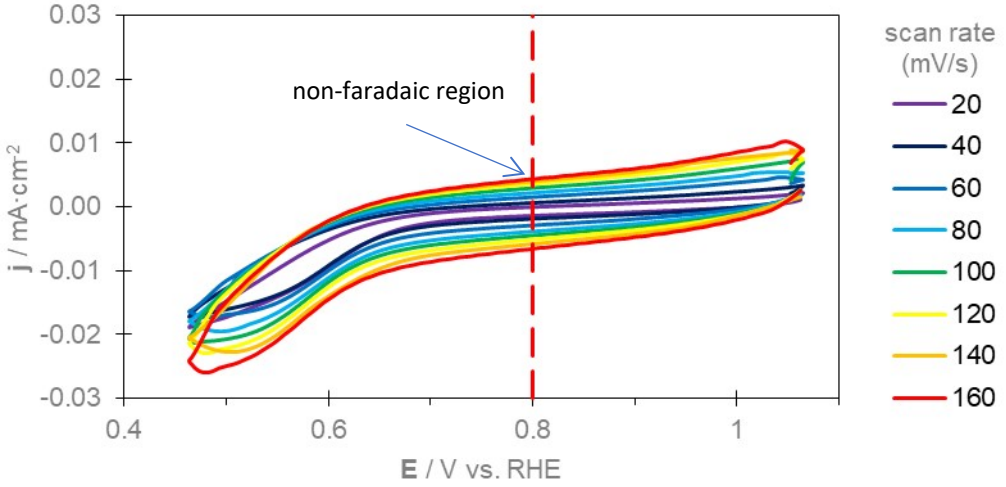

D400

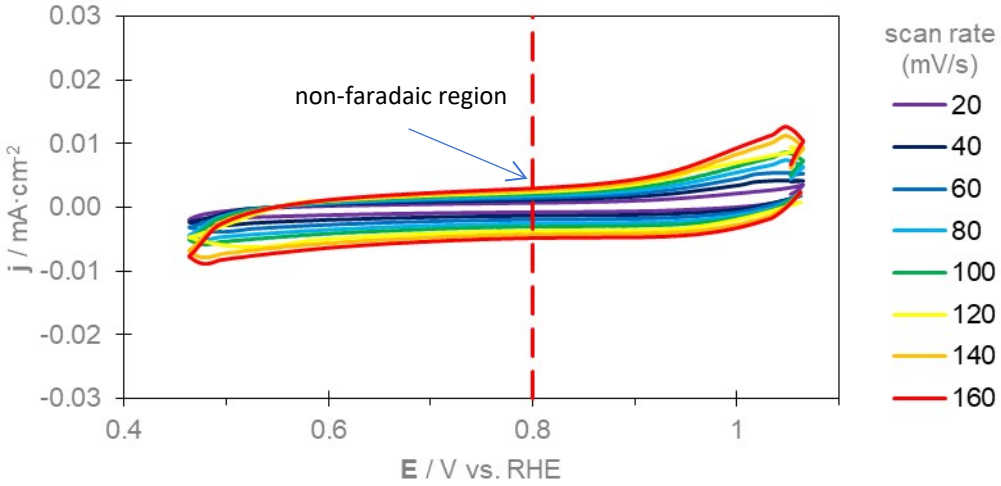

D500

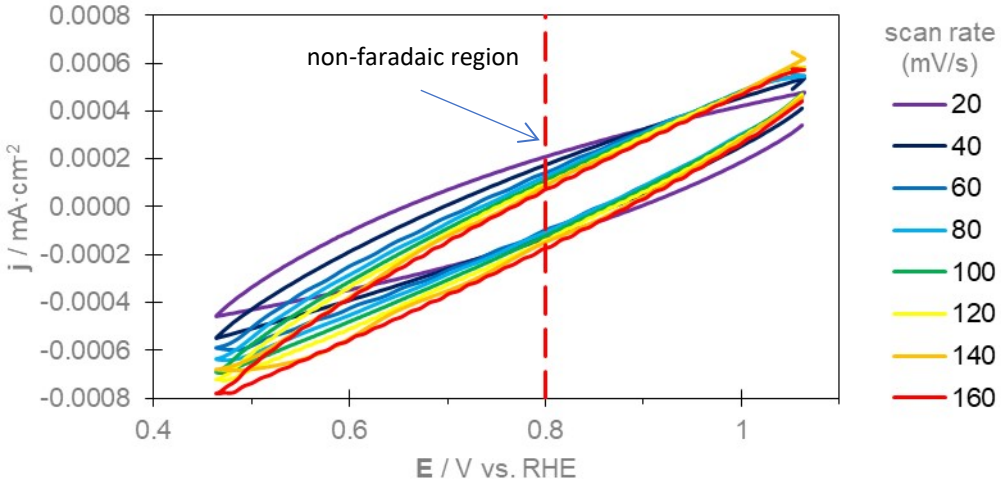

D600

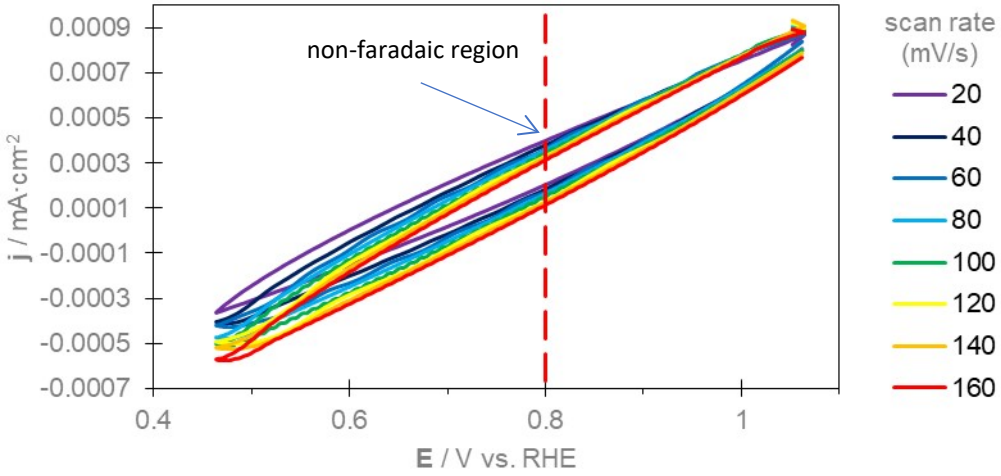

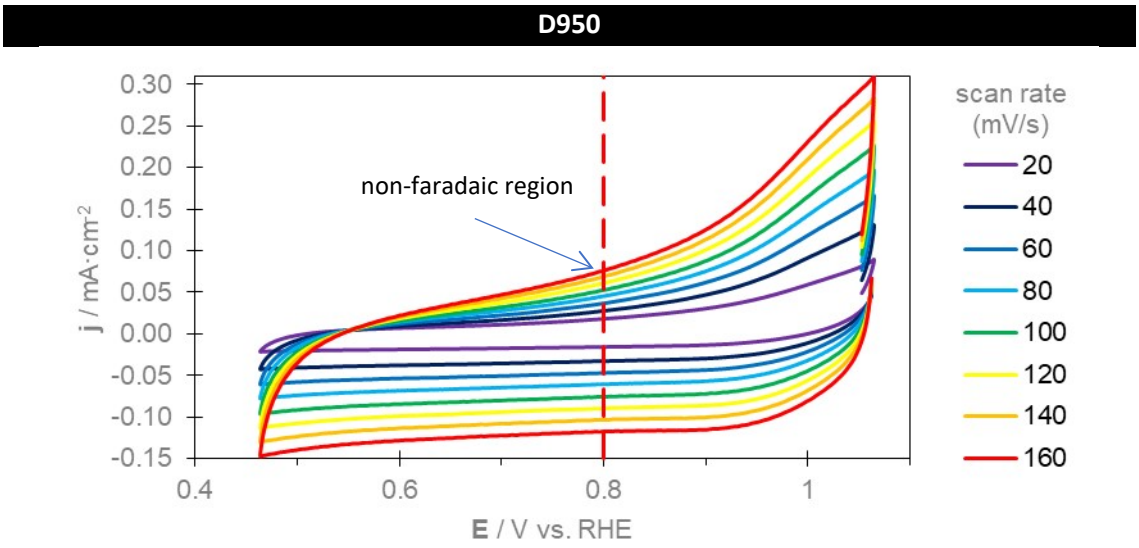

Figure S3. Charge-discharge CV plots at different scan rates (N_2-saturated KOH 0.1 M electrolyte) for the "pure" ZIF-67, $PW_{11}Co$@ZIF-67 and their derivatives.

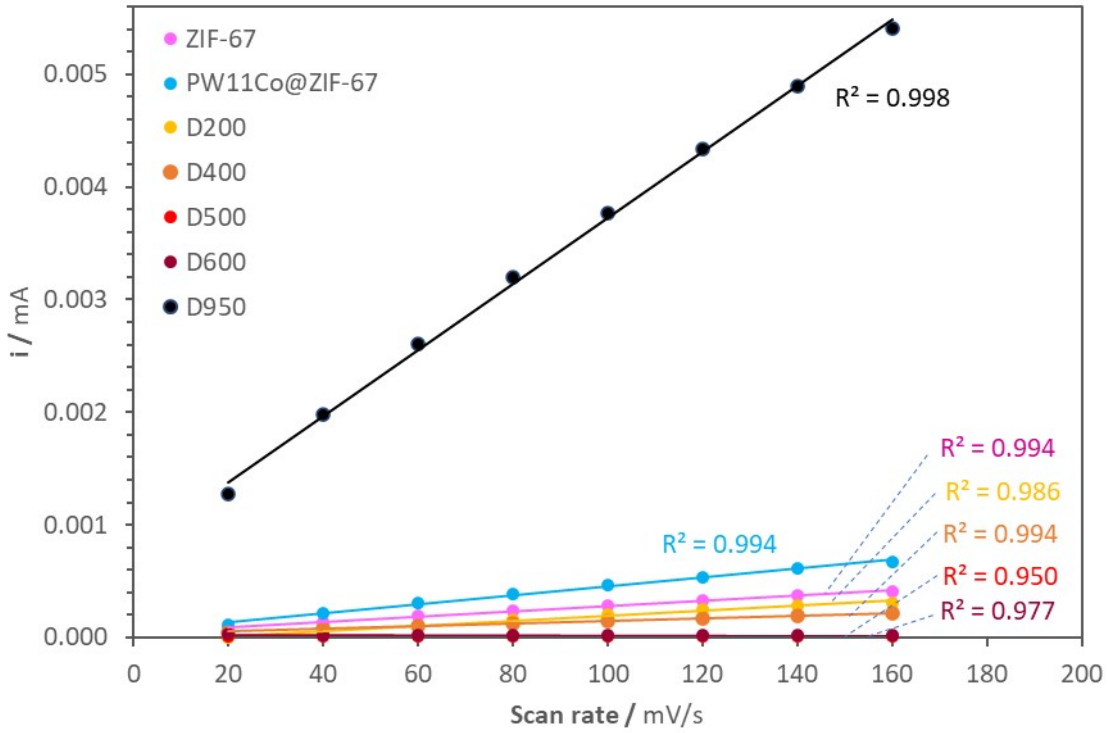

Figure S4. Intensity *vs.* scan rate linear fitting plots derived from the corresponding CV plots (see Fig. S3) for the "pure" ZIF-67, $PW_{11}Co$@ZIF-67 and their derivatives. The slope values, corresponding to C_{dl} parameters are included in Table S7.

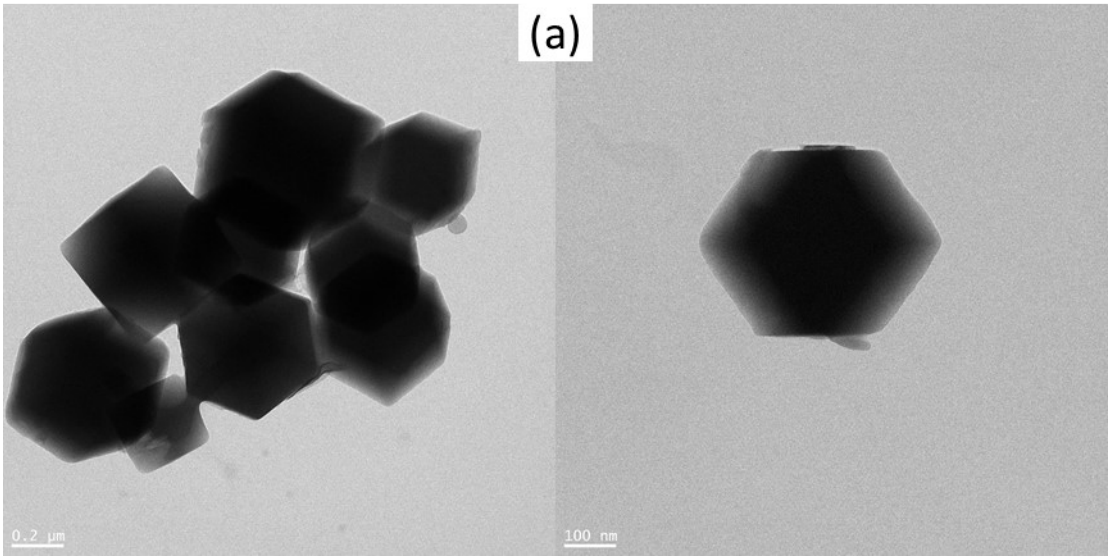
(a)
0.2 µm
100 nm

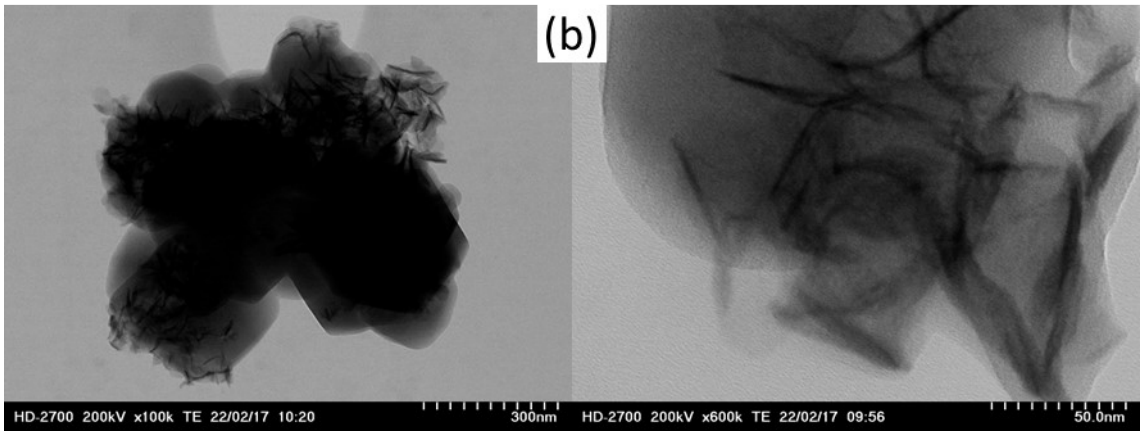
(b)
HD-2700 200kV x100k TE 22/02/17 10:20
300nm
HD-2700 200kV x600k TE 22/02/17 09:56
50.0nm

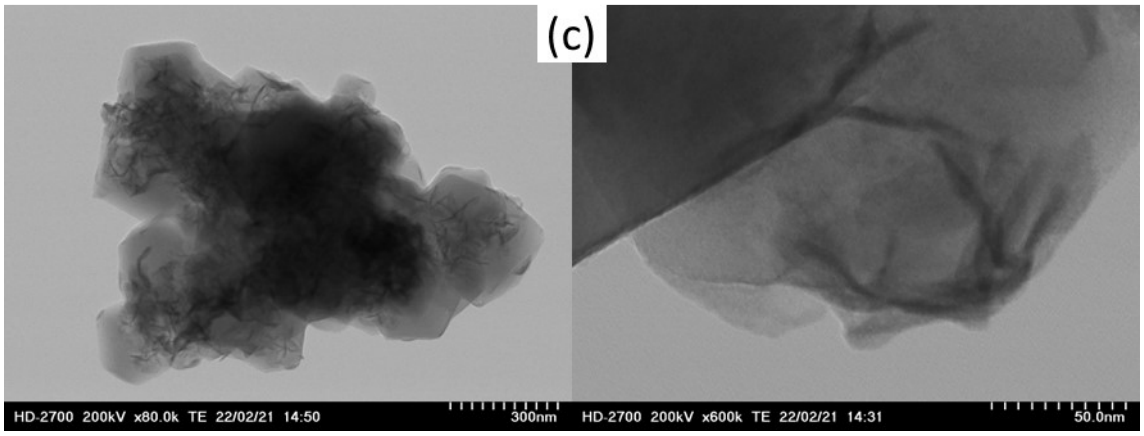
(c)
HD-2700 200kV x80.0k TE 22/02/21 14:50
300nm
HD-2700 200kV x600k TE 22/02/21 14:31
50.0nm

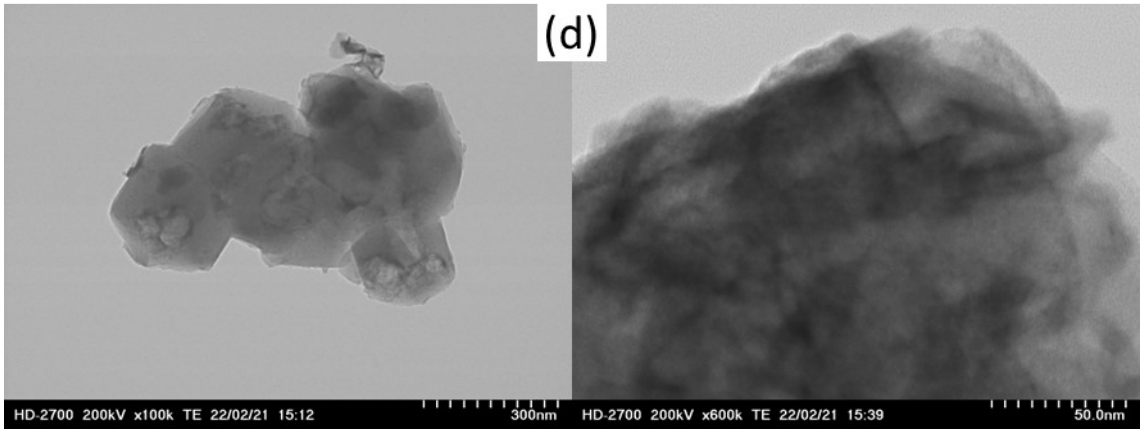
(d)
HD-2700 200kV x100k TE 22/02/21 15:12
300nm
HD-2700 200kV x600k TE 22/02/21 15:39
50.0nm

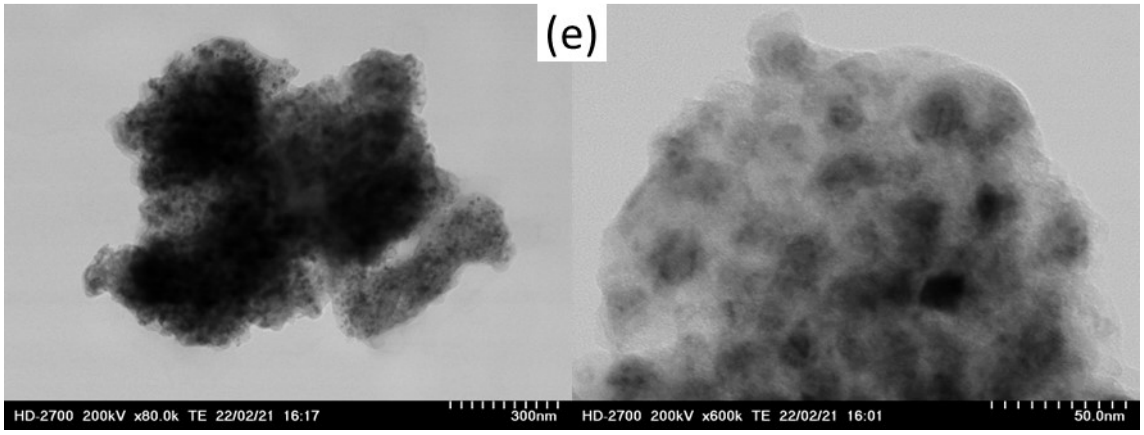
(e)
HD-2700 200kV x80.0k TE 22/02/21 16:17
300nm
HD-2700 200kV x600k TE 22/02/21 16:01
50.0nm

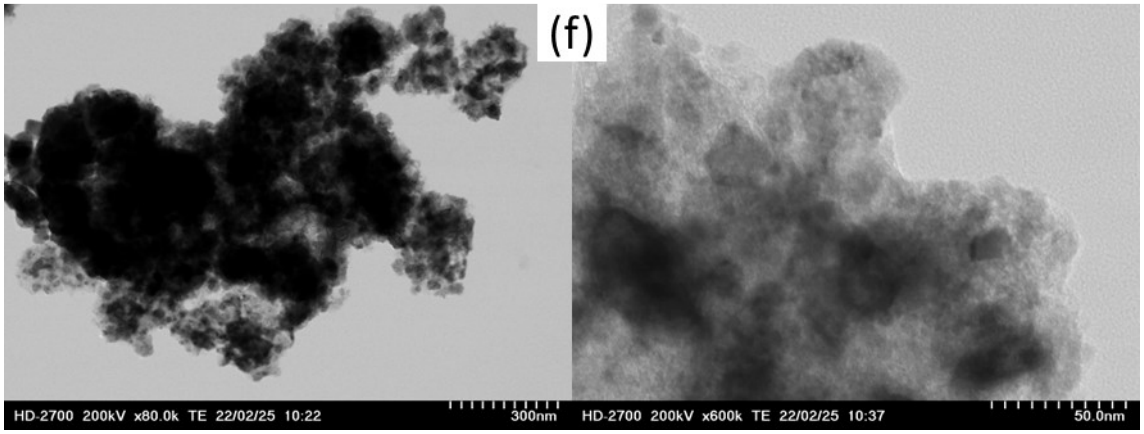
(f)
HD-2700 200kV x80.0k TE 22/02/25 10:22
300nm
HD-2700 200kV x600k TE 22/02/25 10:37
50.0nm

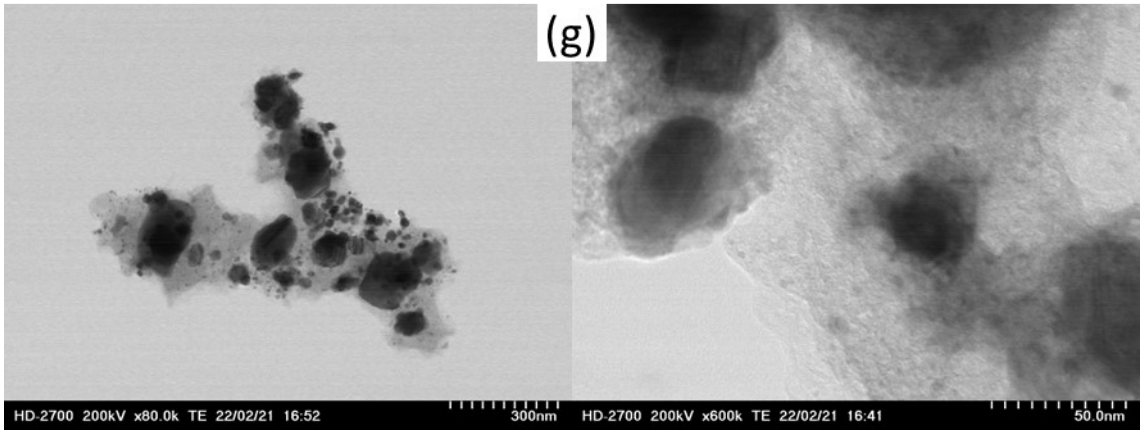
(g)
HD-2700 200kV x80.0k TE 22/02/21 16:52
300nm
HD-2700 200kV x600k TE 22/02/21 16:41
50.0nm

Figure S5. TEM images for **(a)** ZIF-67, **(b)** $PW_{11}Co$@ZIF-67, **(c)** D200, **(d)** D400, **(e)** D500, **(f)** D600, and **(g)** D950.

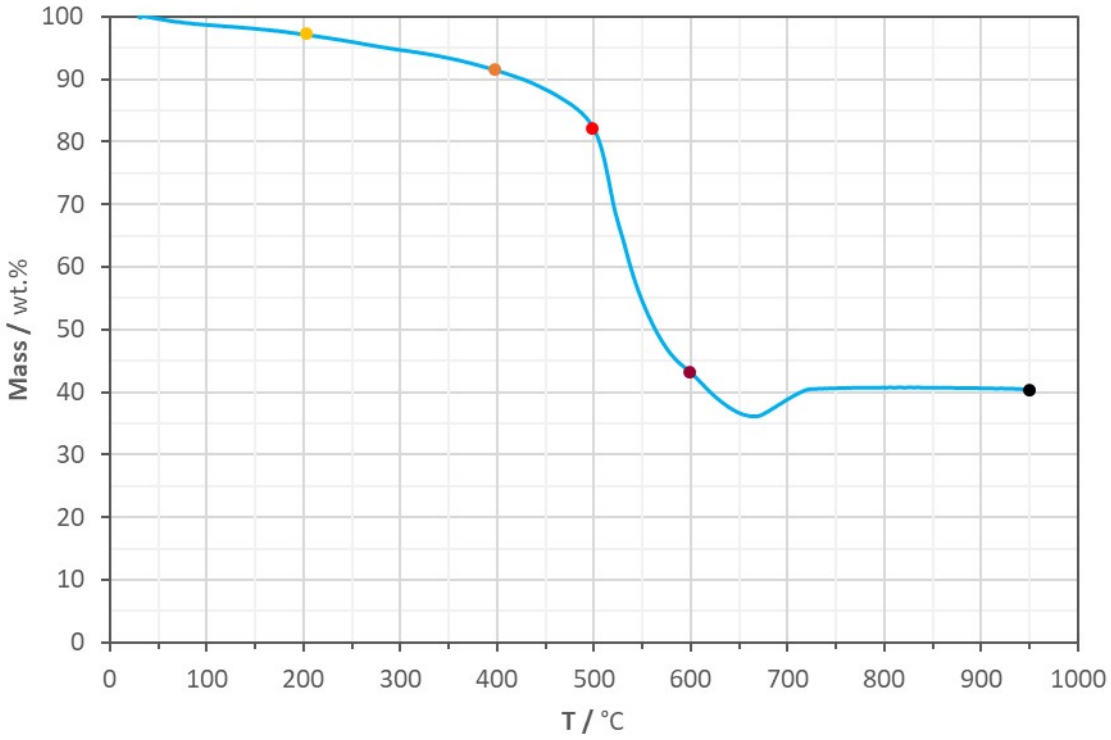

Figure S6. TGA curve of the $PW_{11}Co$@ZIF-67 precursor (registered in N_2 flow). Temperatures selected for the thermal treatments are highlighted.

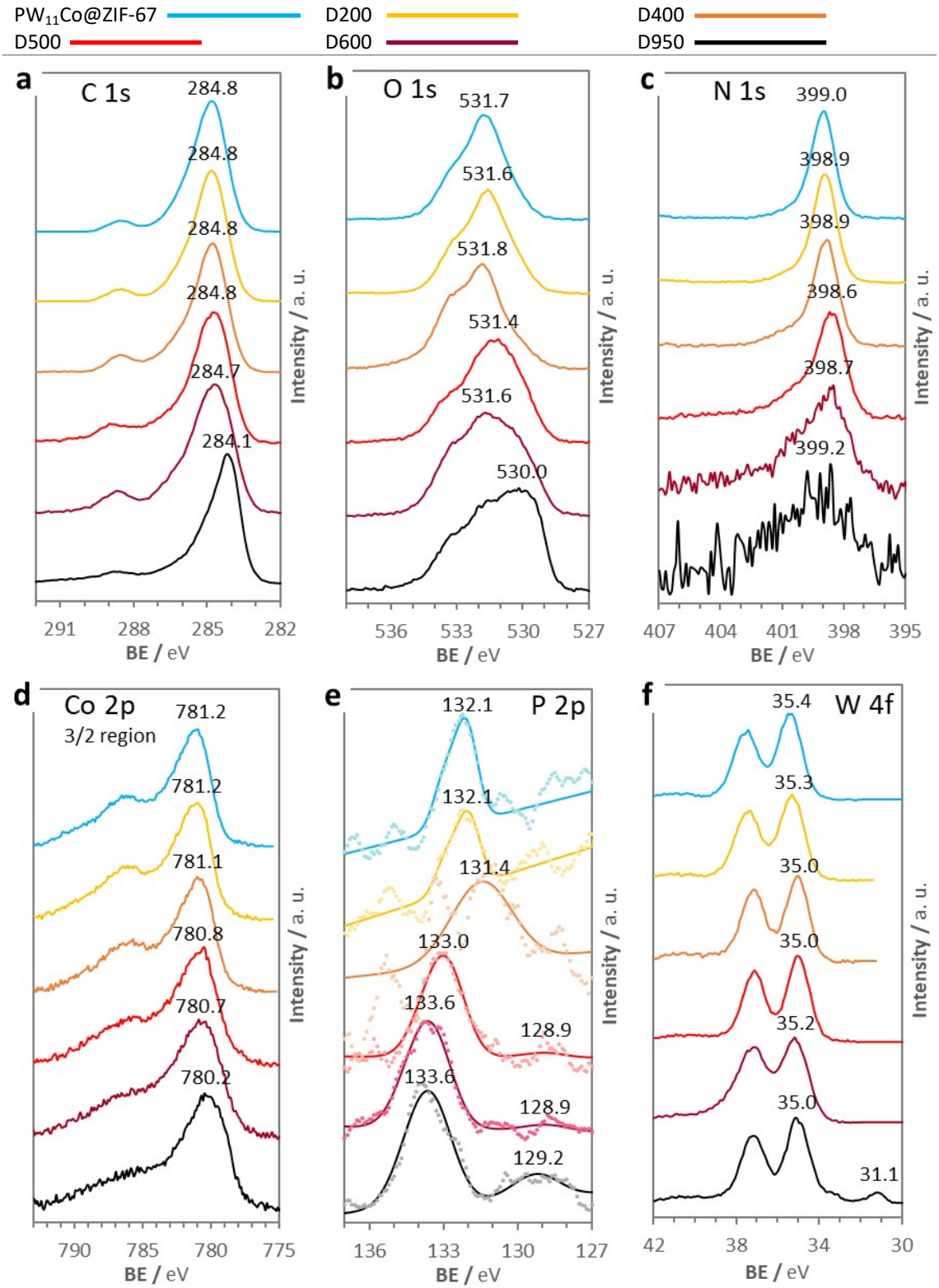

Figure S7. Profiles of high-resolution XPS core-level spectra for $PW_{11}Co$@ZIF-67 and its derivatives: **(a)** C 1s, **(b)** O 1s, **(c)** N 1s, **(d)** Co 2p —3/2 region—, **(e)** P 2p, and **(f)** W 4f regions. *In (e), the deconvolution fitted envelopes have been included as solid lines due to the elevated noise-to-signal ratio of the raw data (indicated with light-colored spots) originated by the extremely low P concentrations in the samples (see Table 2).*

C 1s peak profiles in **Fig. S7a** gradually shift to lower binding energy (BE) values with increasing temperatures, adopting, especially in D950, the characteristic sharpened asymmetric profile of graphitic carbon materials.[19] O 1s peaks (**Fig. S7b**) also progressively change from a more defined profile produced by the combination of O atoms from the $PW_{11}Co$ cluster and from adventitious carbon[5] to a broadened irregular band, usually generated by the presence of diverse oxygen-containing functional groups in carbon materials. In addition, the growth of the signal peak in the region around 530 eV observed in D500, D600, and D950, indicates the formation of metal oxides, probably CoO and WO_x ($2 \leq x \leq 3$).[20] Regarding the N 1s region, N 1s peaks of D600 and D950 (**Fig. S7c**) show elevated noise levels due to the low nitrogen concentration in these samples, 2.6 and 1.4 at.%, respectively. Besides, they widen compared to those of the previous samples, adopting the typical profile for the co-existence of different N moieties doping the graphenic carbon domains.[21] The shifting of Co 2p peaks (**Fig. S7d**) to lower BE values denotes the gradual increase of the reduced Co^0 proportion in the samples treated at higher T.[11] Focusing on P 2p profiles (**Fig. S7e**), the P 2p core-level regions from D500 onwards involve two differentiated peaks, one predominant associated with metal phosphates (at 133.6–133.0 eV), and another one ascribable to metal phosphides (at ≈129 eV), probably to CoP.[18] Finally, W 4f peaks in **Fig. S7f** can be assigned to the W-O bonds of $PW_{11}Co$ in $PW_{11}Co$@ZIF-67, D200, and D400, and to WO_x ($2 \leq x \leq 3$) species —originated by the high-temperature treatments— in D500, D600, and D950. In this last sample, a new low-intensity peak appears at ≈31 eV, indicating the presence of a minor amount of reduced tungsten (W^0).[20, 22]

$PW_{11}Co$ “pristine”

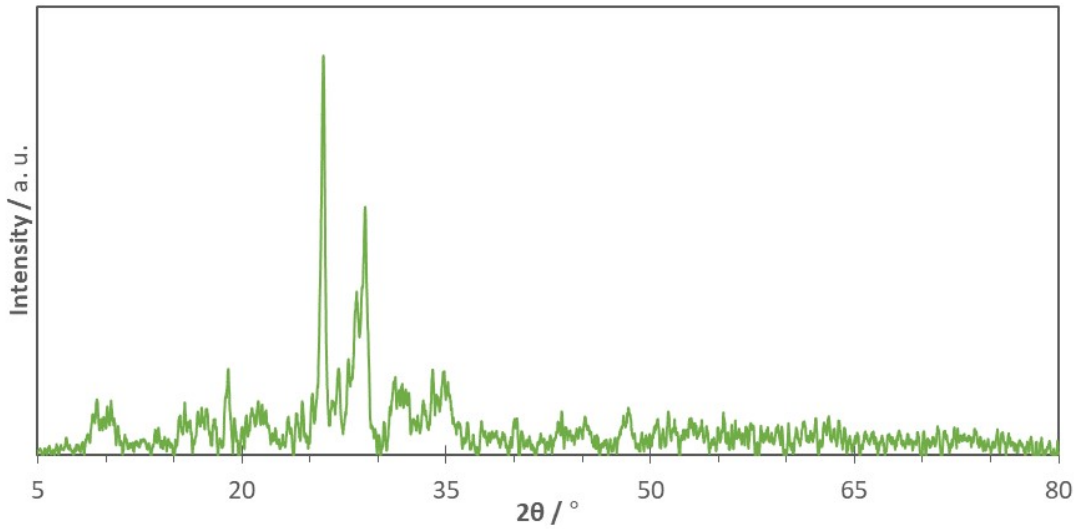

ZIF-67 “pristine”

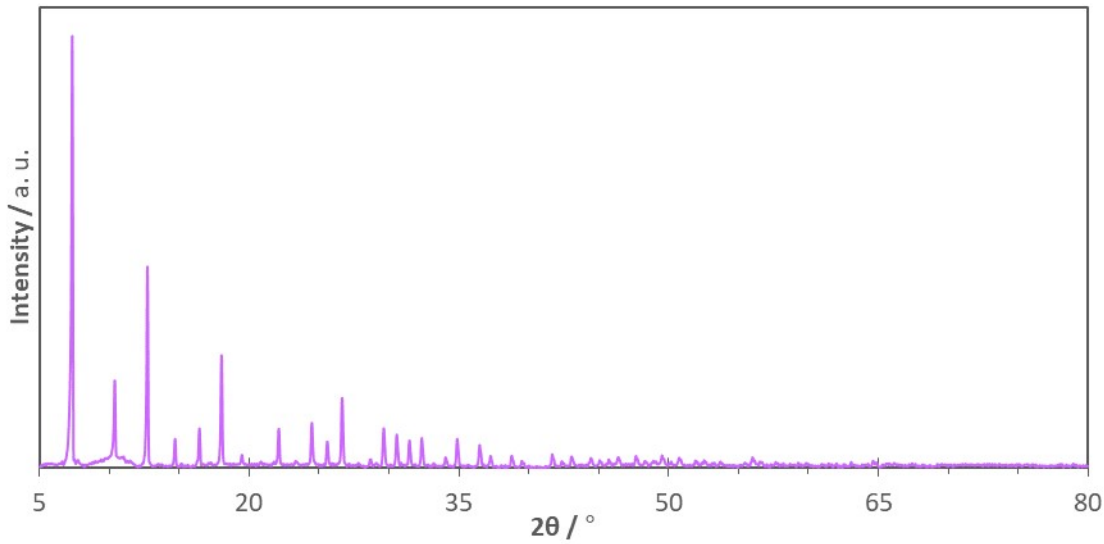

$PW_{11}Co$@ZIF-67

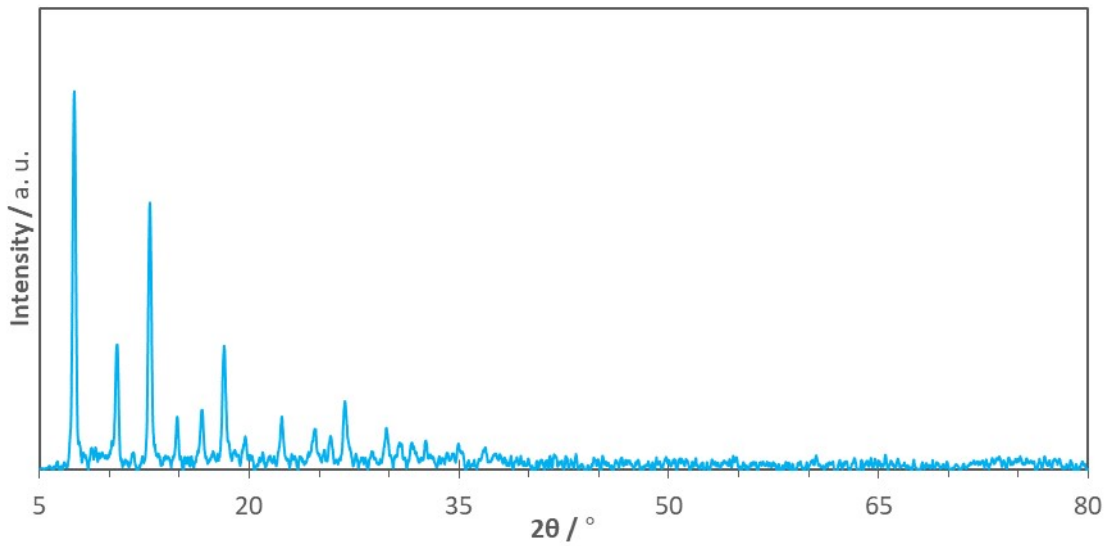

D200

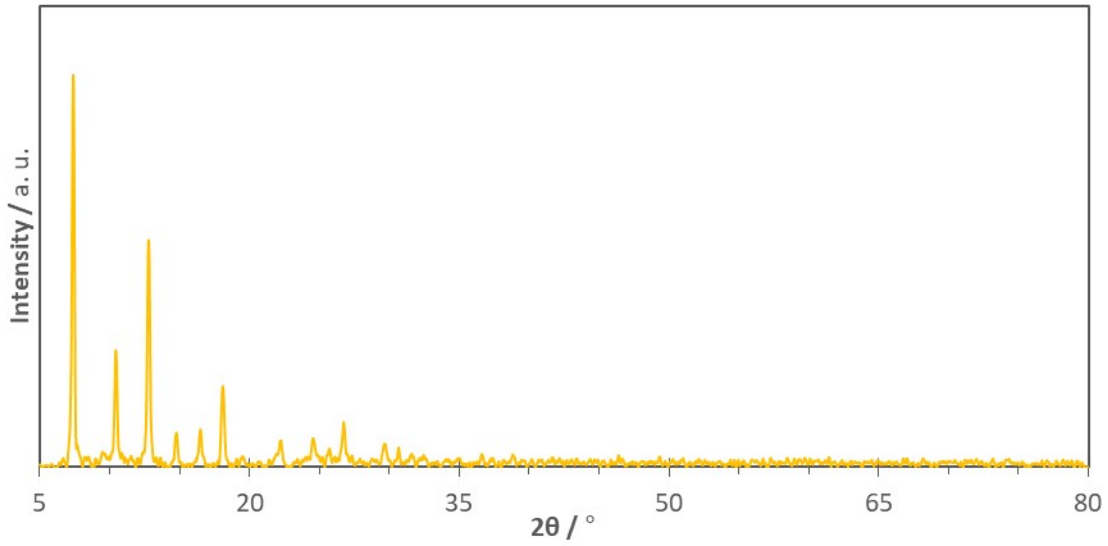

D400

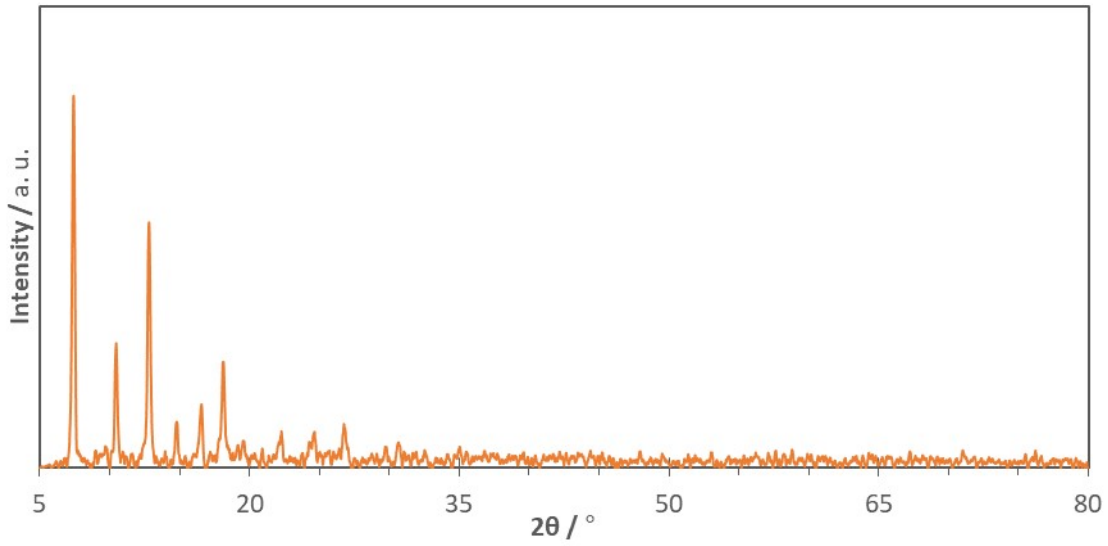

D500

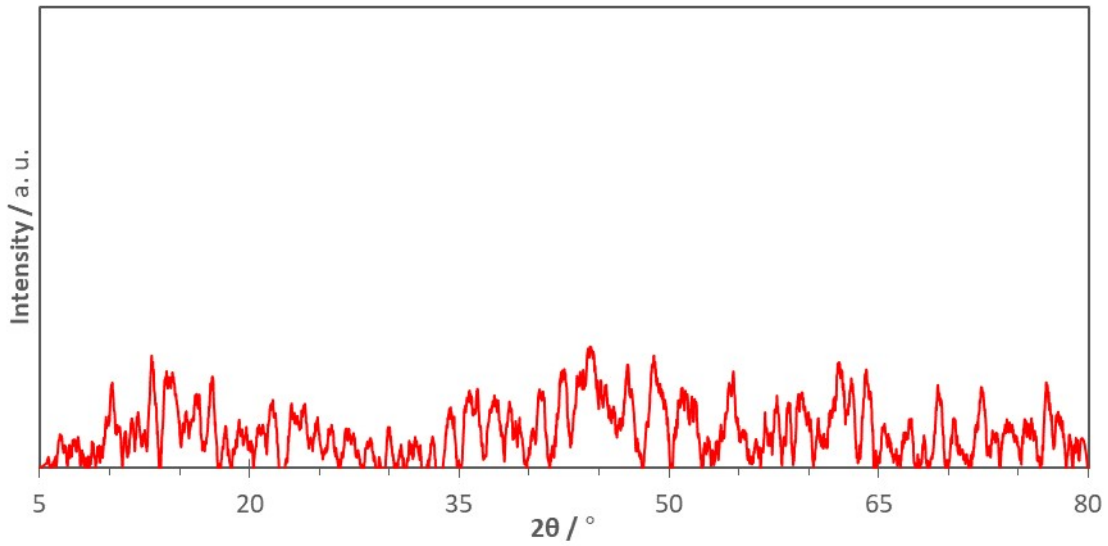

D600

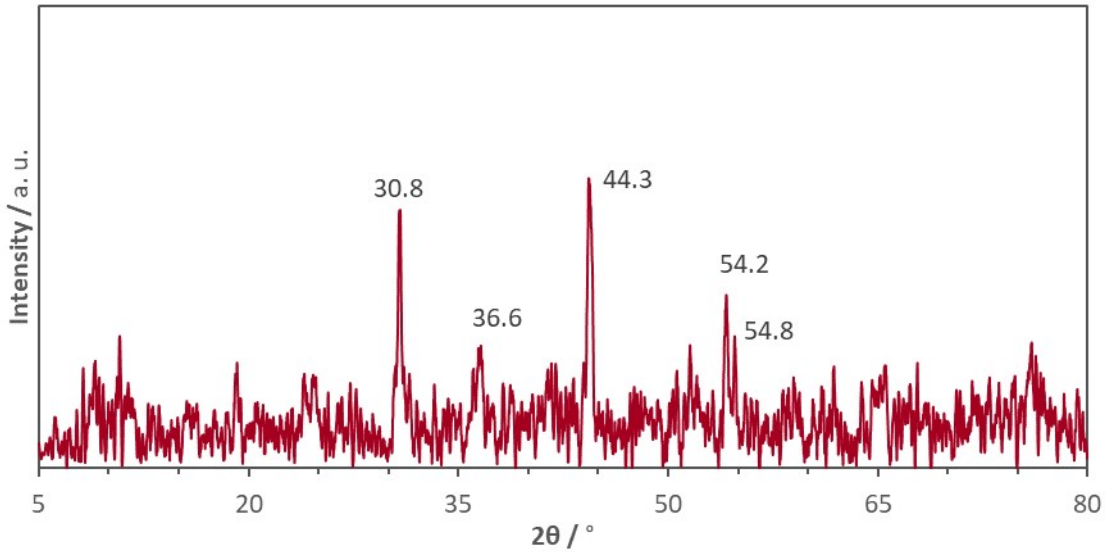

Peak (°)	Tentative assignment
30.8	Co_3O_4 / Co_3P / P_2W
36.6	CoO / CoO_2 / Co_3O_4 / CoP / Co_3P / CoP_2 / WO_2 / W_4P / PW_3
44.3	Co^0
54.2	WO_3 / P_2W / PW_3
54.8	CoP_2 / WO_3 / PW / PW_3

D950

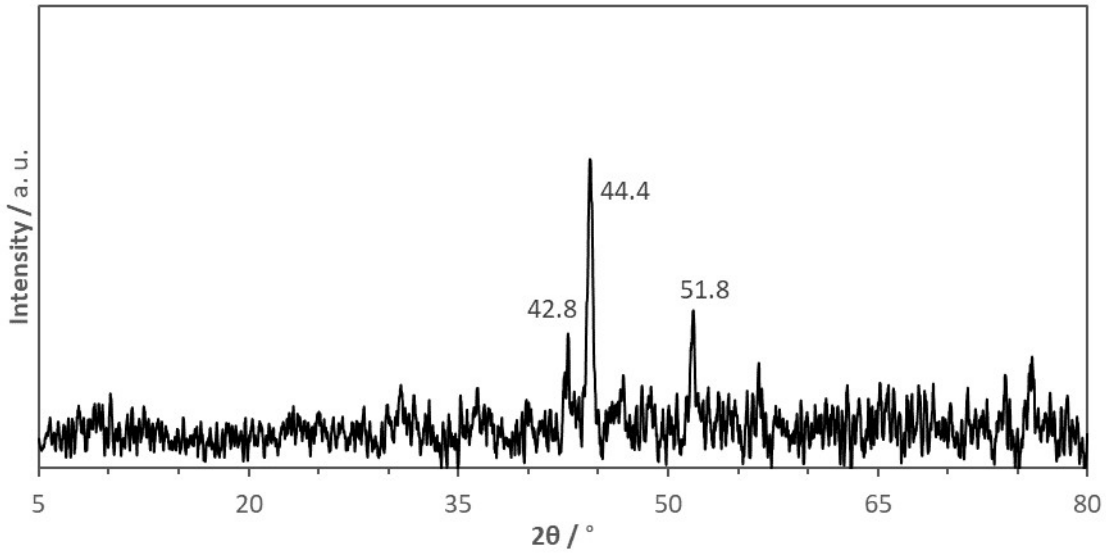

Peak (°)	Tentative assignment
42.8	CoO / CoO_2 / WO_3 / PW / P_2W
44.4	Co^0
51.8	CoP_2 / $W_{11}O_{12}$ / W_3O_8 / PW

Figure S8. PXRD diffractograms of the "pure" $PW_{11}Co$ and ZIF-67, the $PW_{11}Co$@ZIF-67 precursor, and the derived nanocomposites.

$PW_{11}Co$@ZIF-67

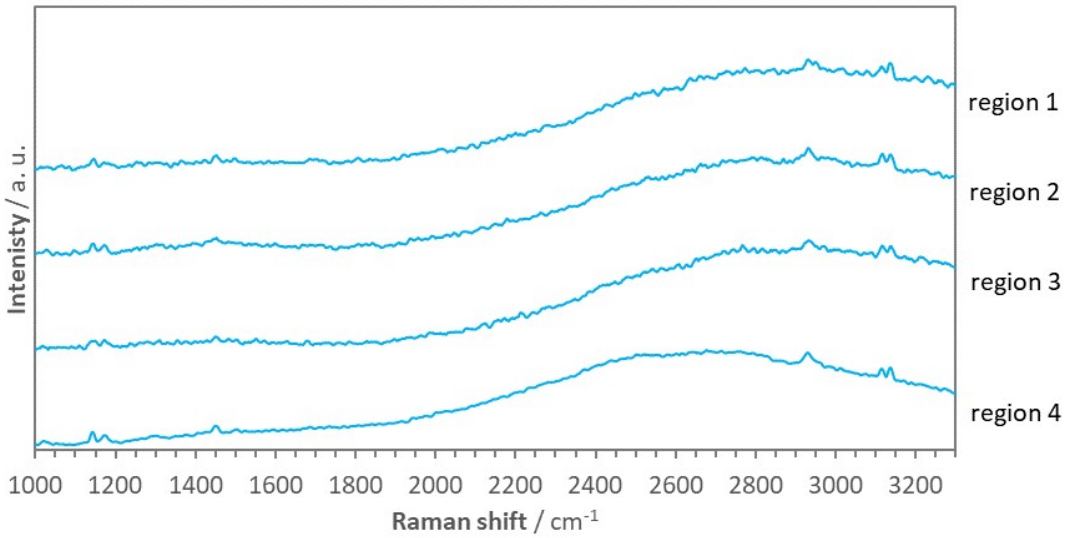

D200

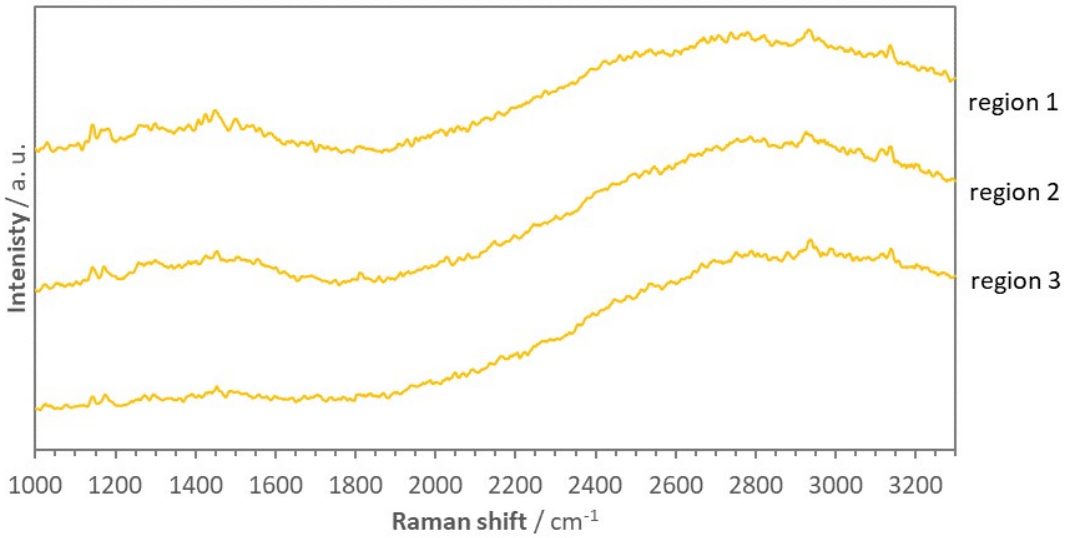

D400

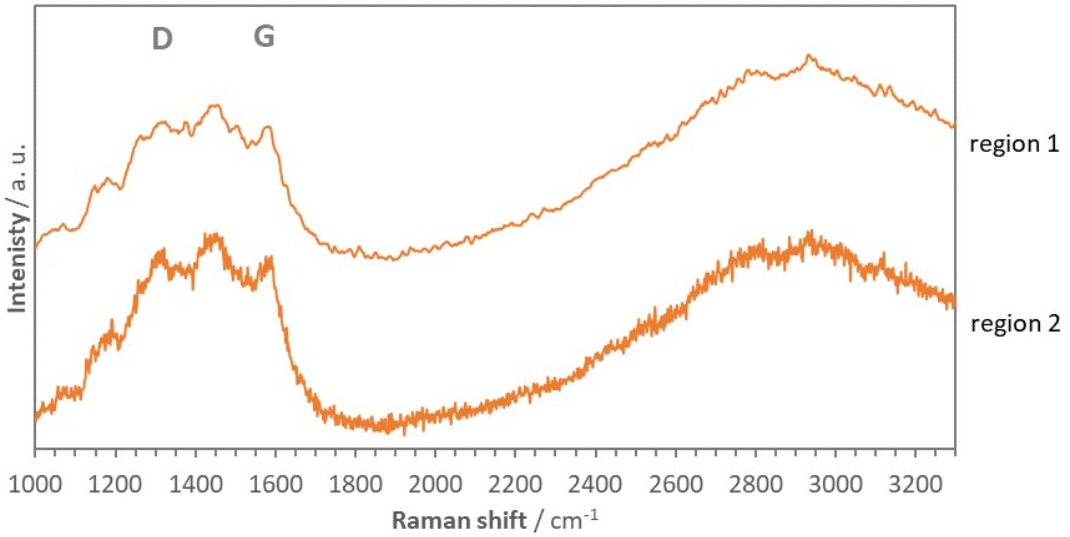

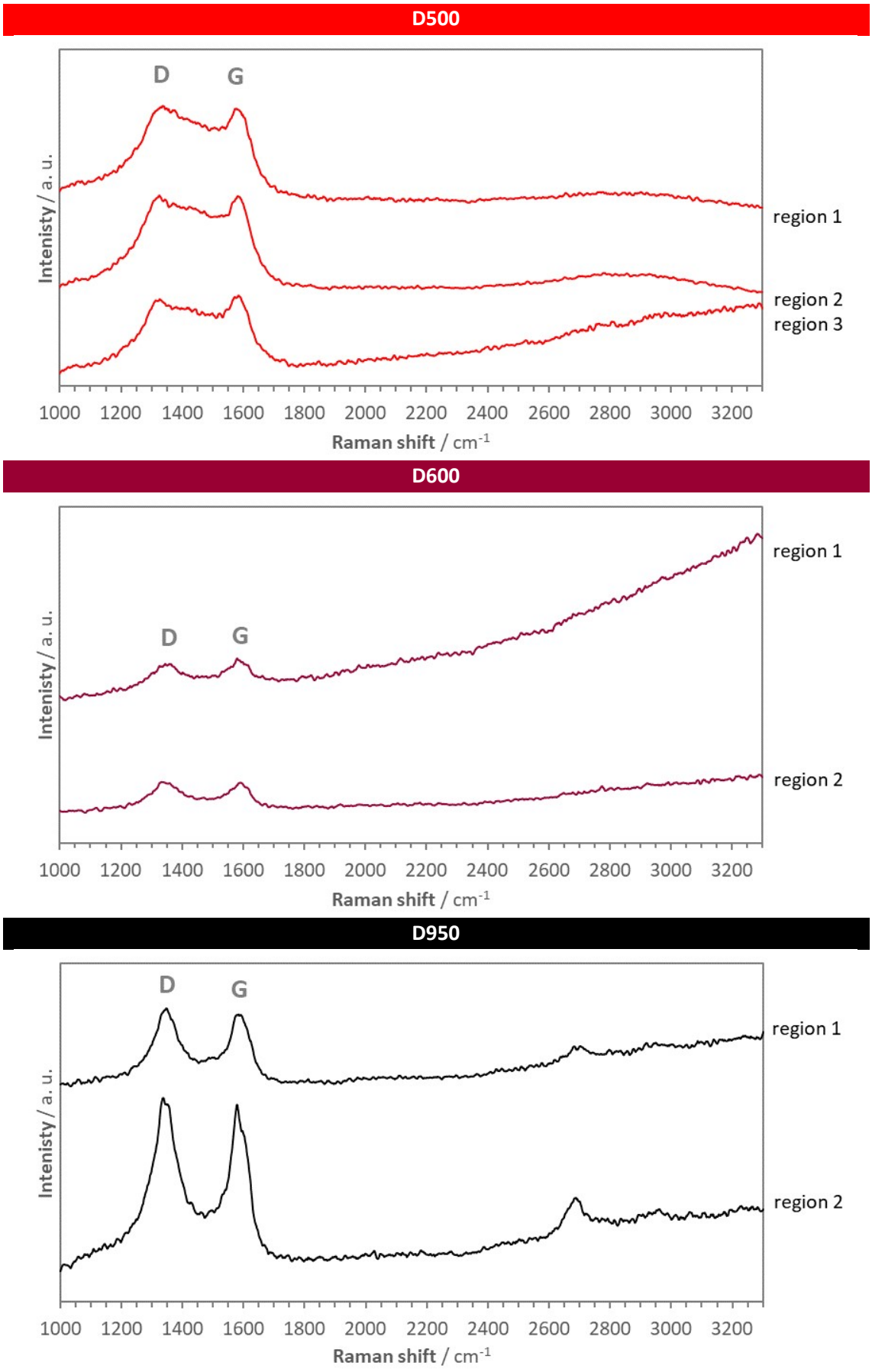

Figure S9. Raman spectra for different regions of $PW_{11}Co$@ZIF-67 and their derivatives.

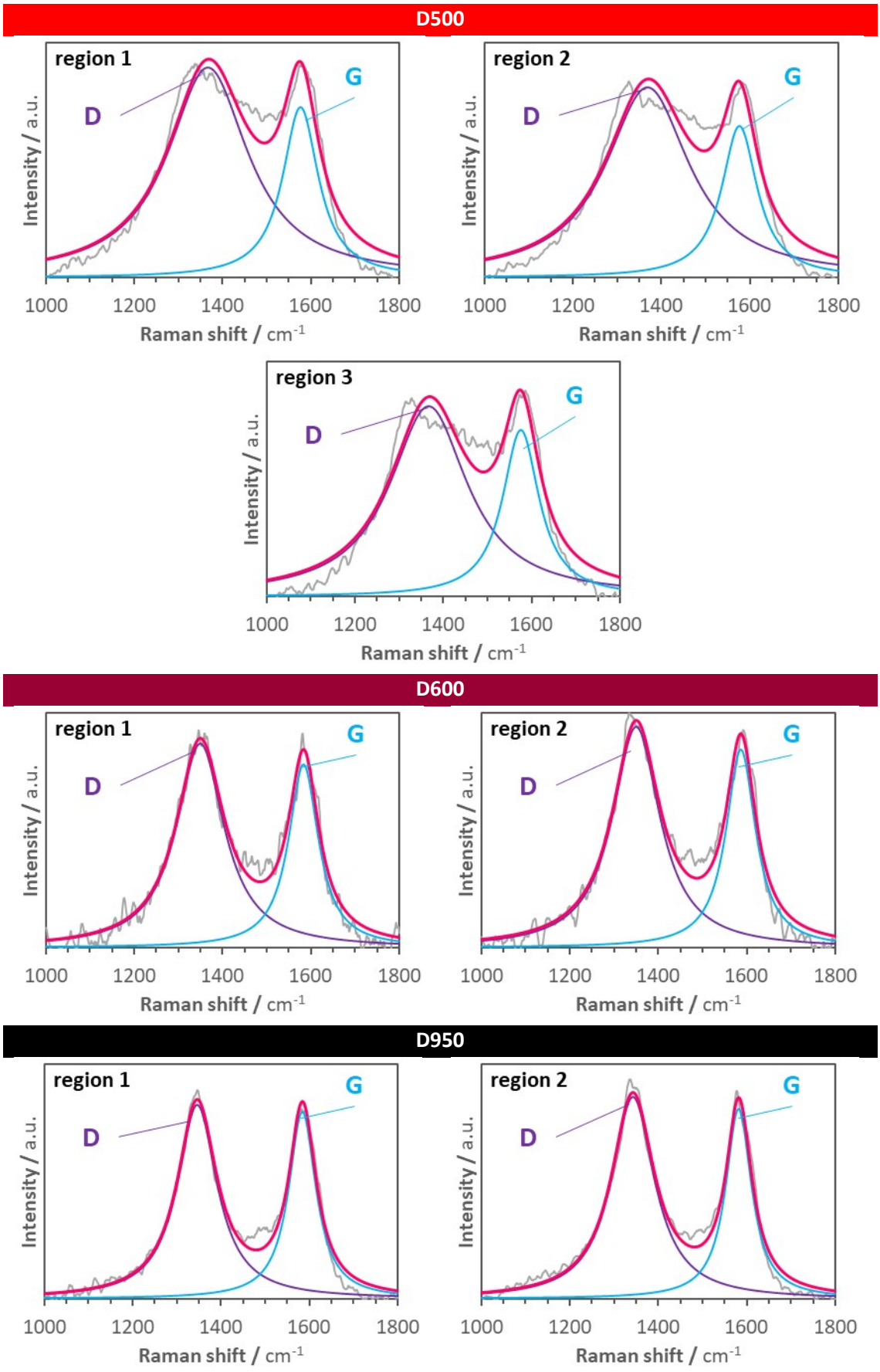

Figure S10. 2-component deconvolutions of Raman spectra (1000-1800 cm^{-1} region) for the carbonaceous derivatives: D500, D600, and D950.

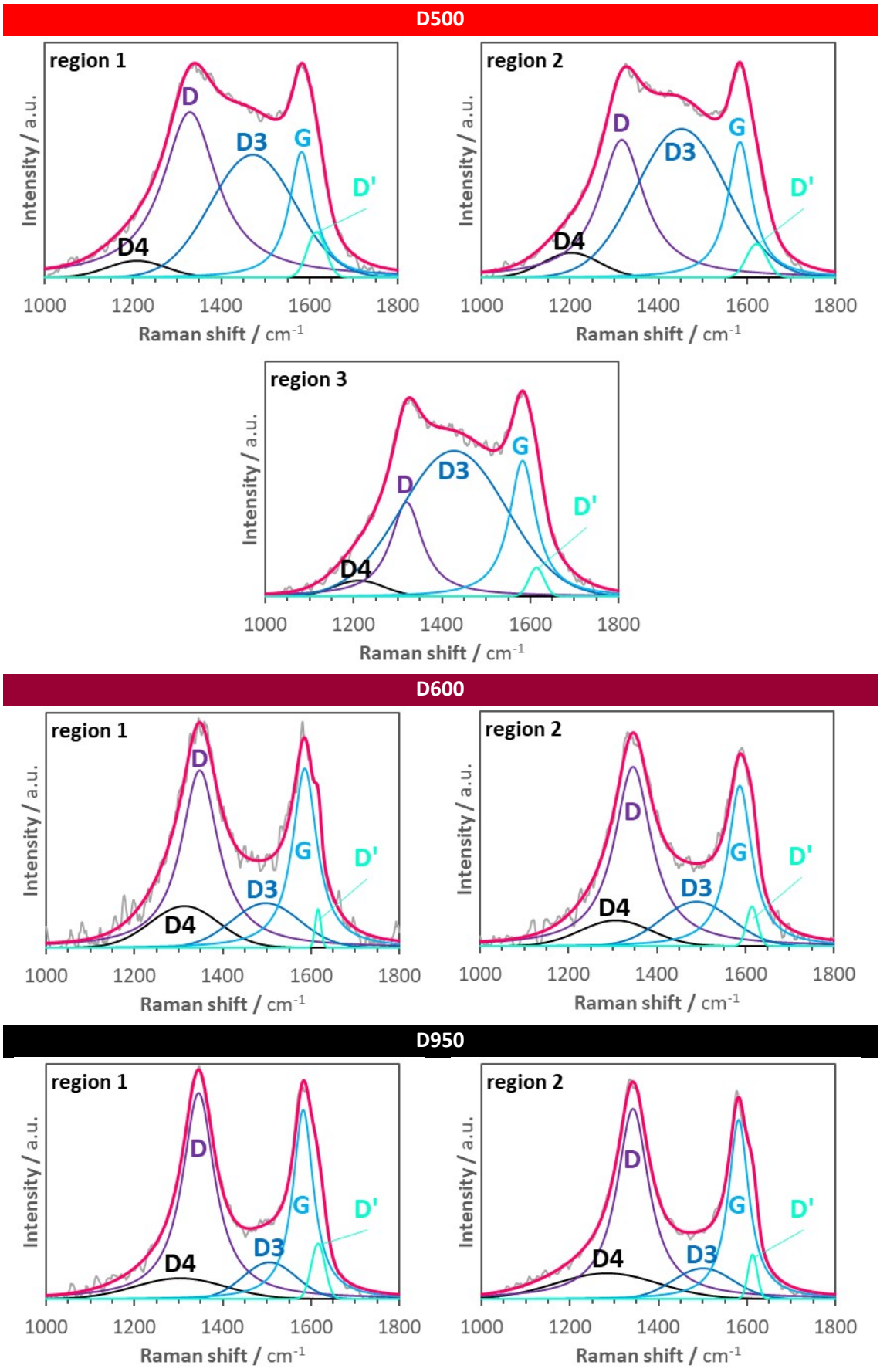

Figure S11. 5-component deconvolutions of Raman spectra (1000-1800 cm^{-1} region) for the carbonaceous derivatives: D500, D600, and D950.

$PW_{11}Co$@ZIF-67

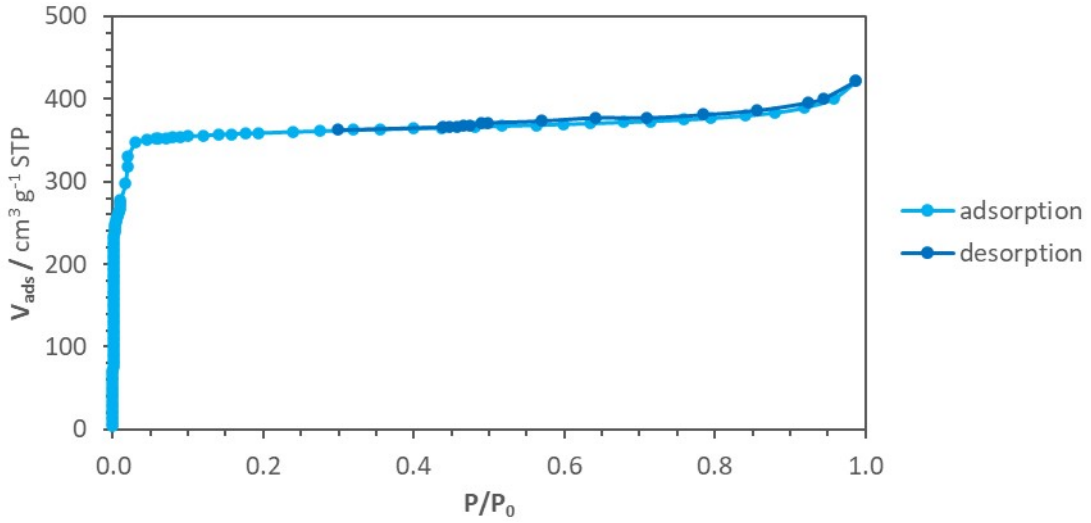

D200

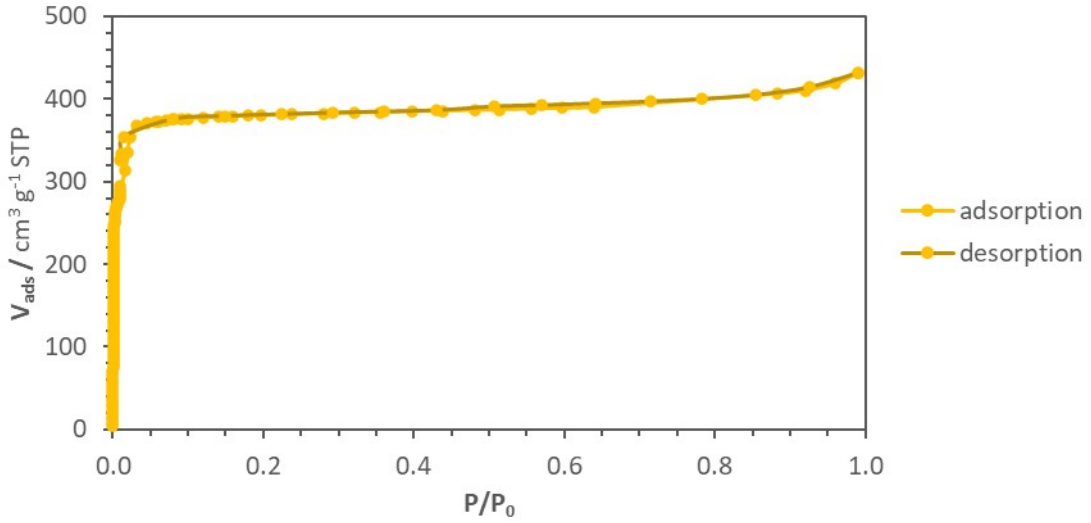

D400

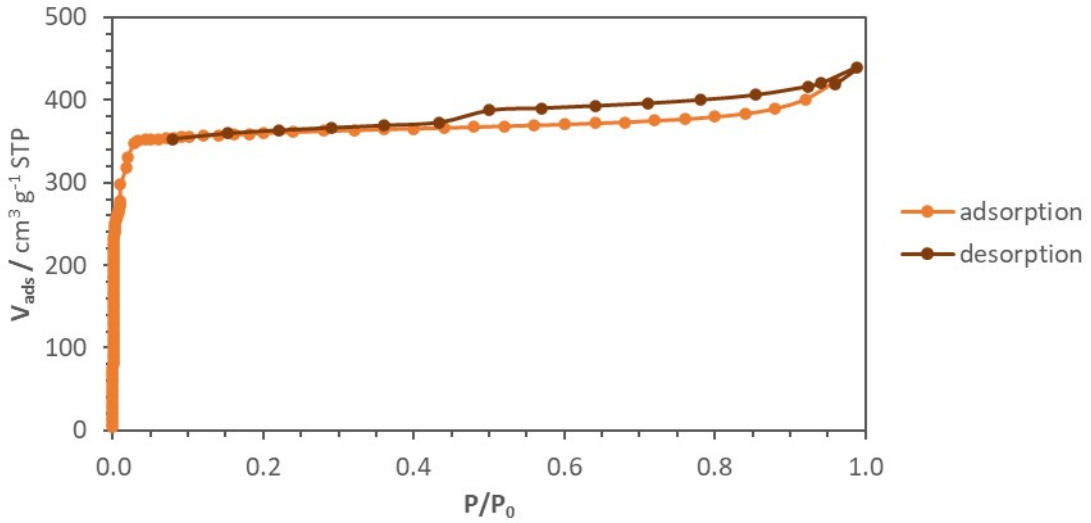

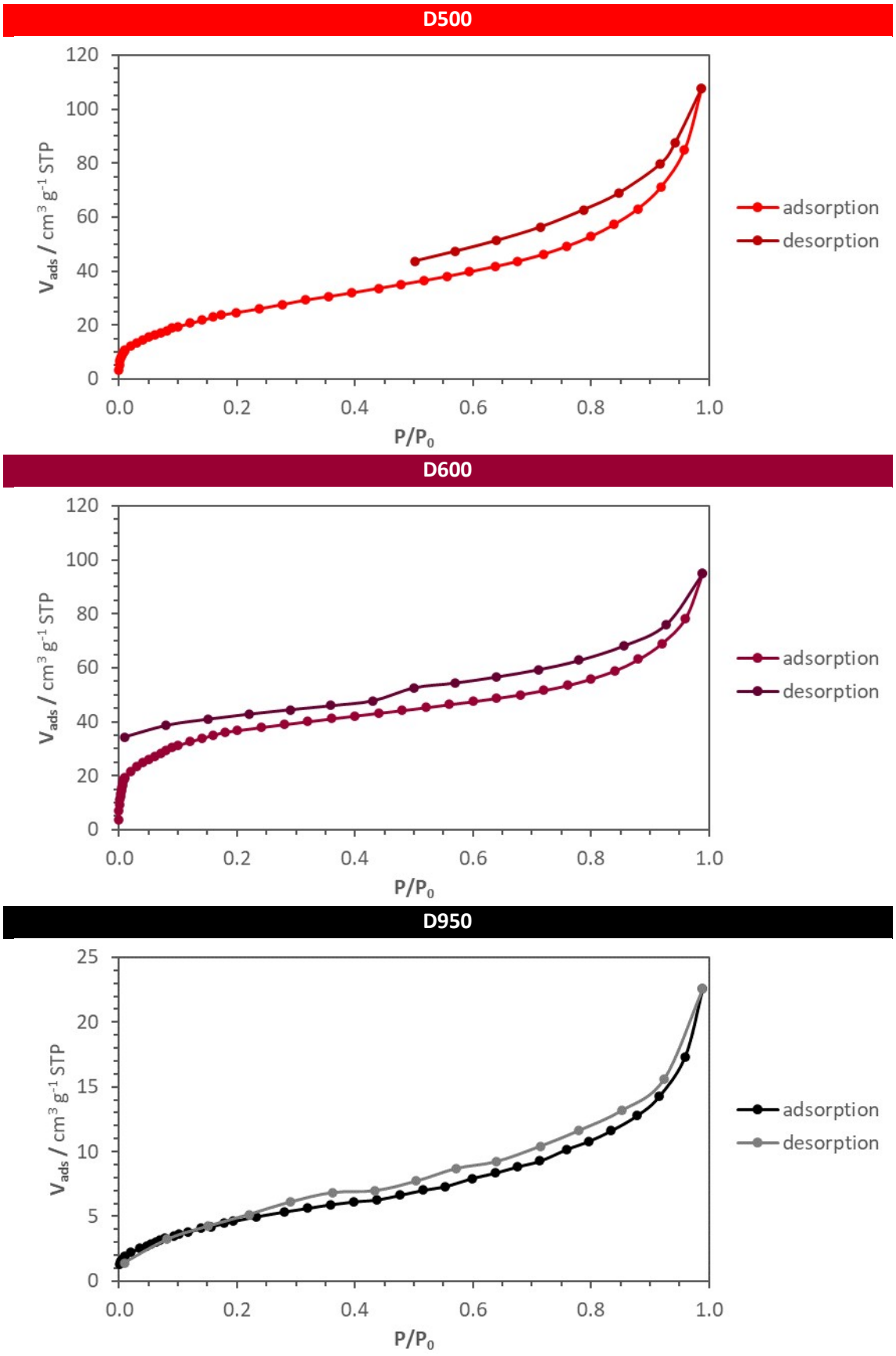

Figure S12. Nitrogen adsorption-desorption isotherms for $PW_{11}Co$@ZIF-67 and their derivatives.

$PW_{11}Co$@ZIF-67

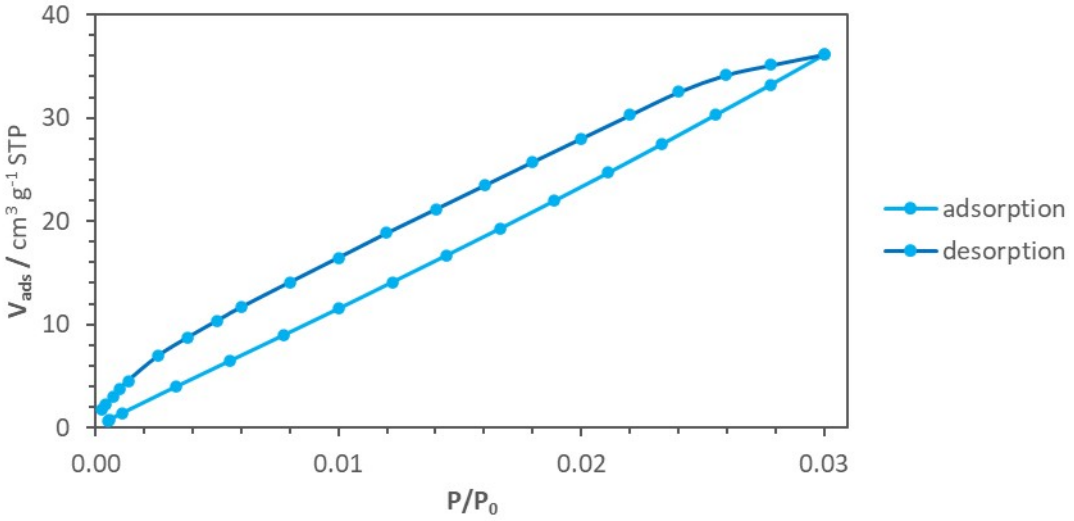

D200

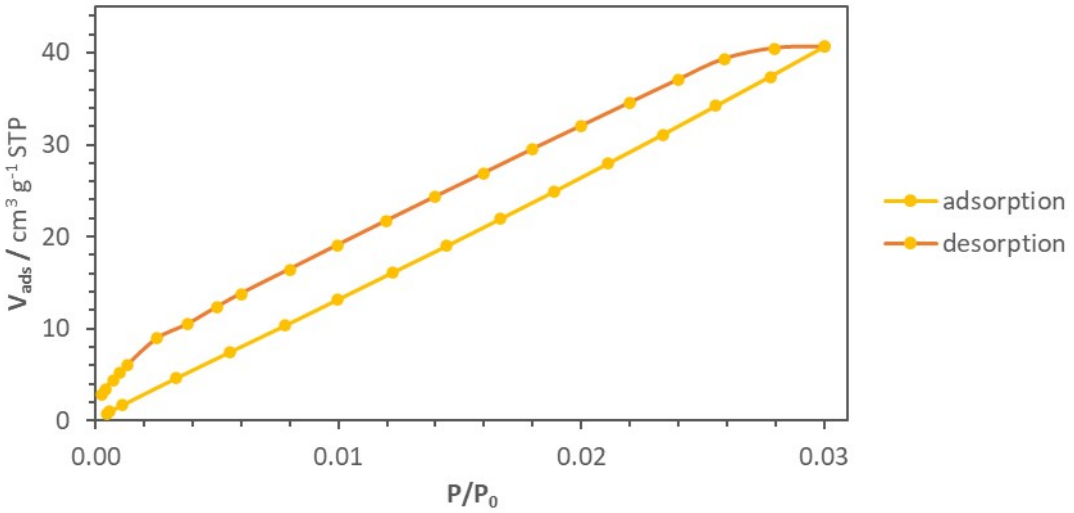

D400

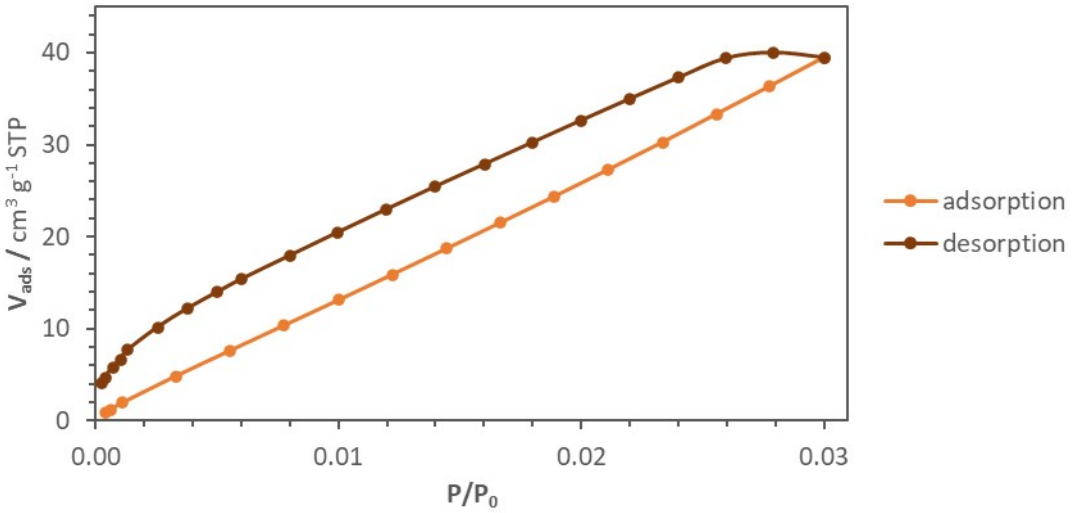

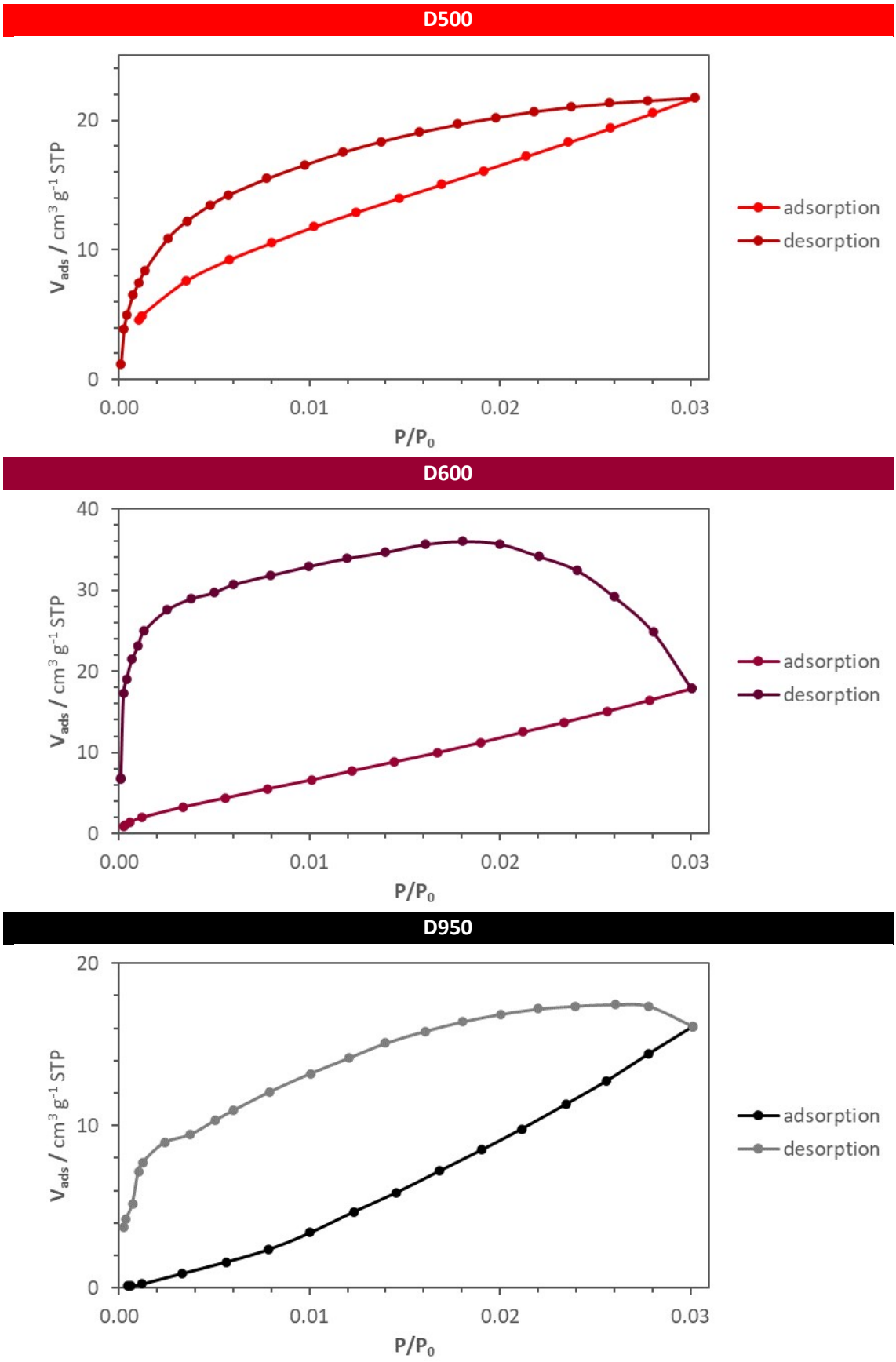

Figure S13. Carbon dioxide adsorption-desorption isotherms for $PW_{11}Co$@ZIF-67 and their derivatives.

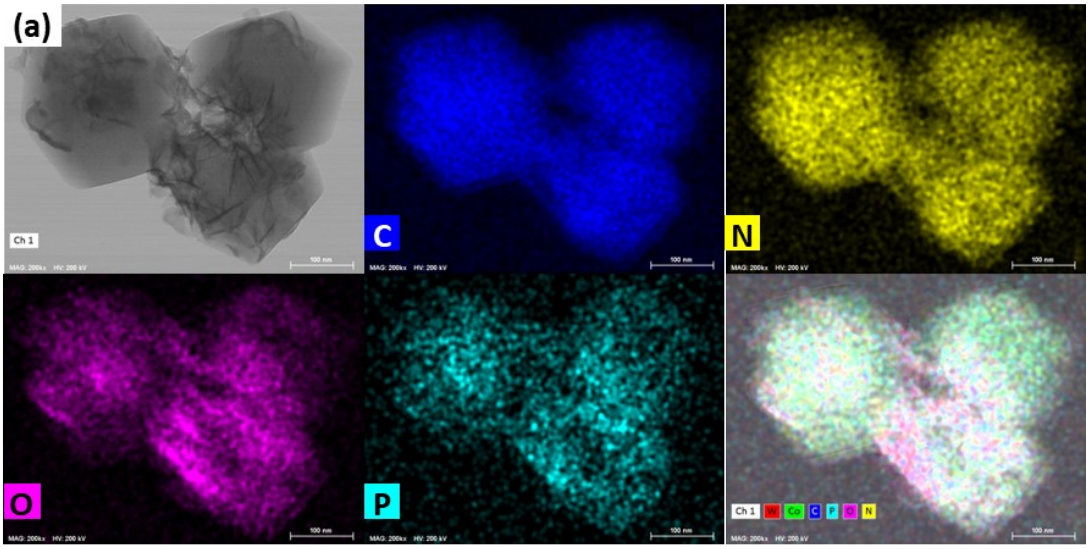
(a)
Ch 1
C
N
O
P
Ch 1

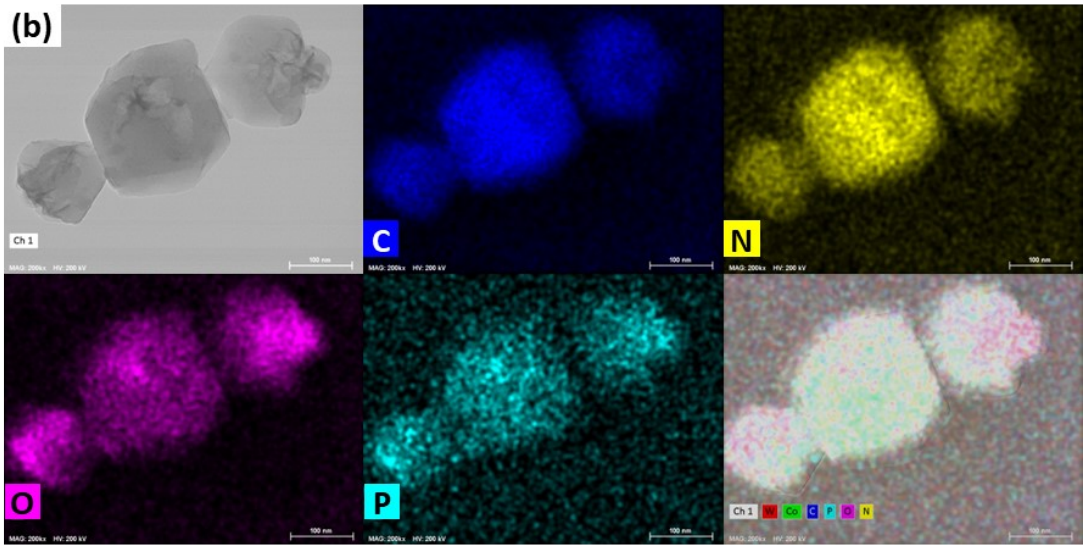
(b)
Ch 1
C
N
O
P
Ch 1

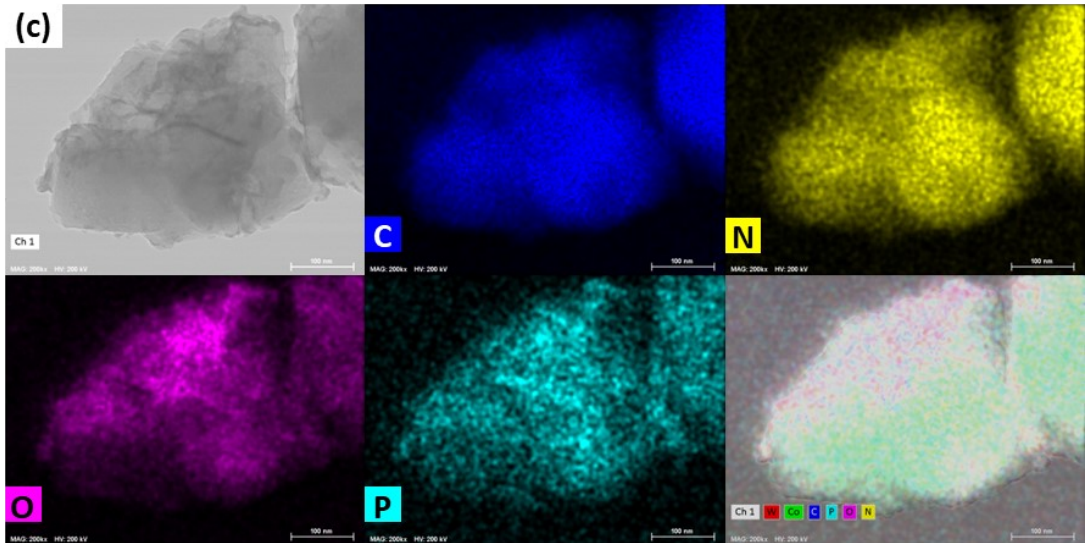
(c)
Ch 1
C
N
O
P
Ch 1

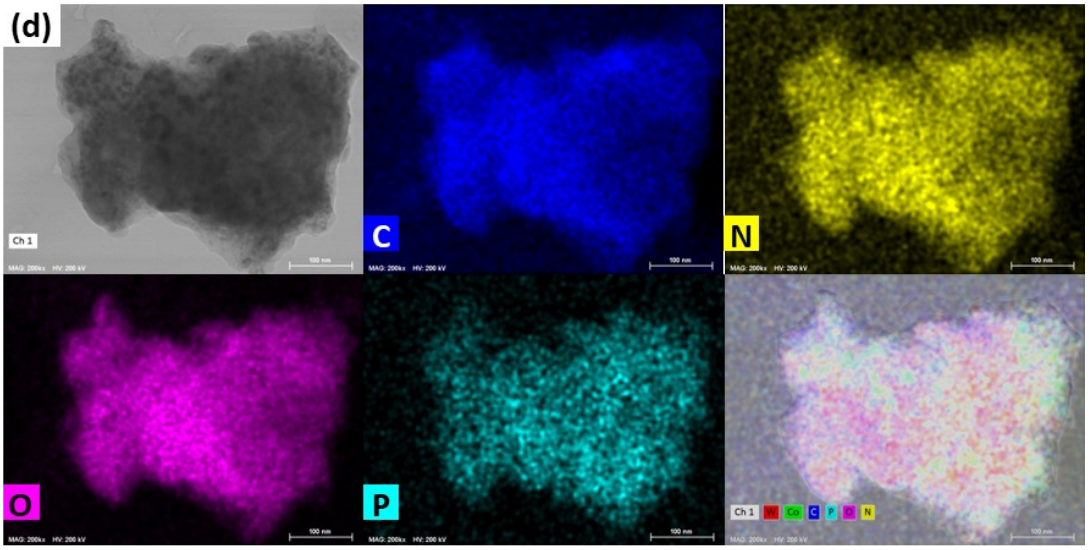
(d)
Ch 1
C
N
O
P
Ch 1

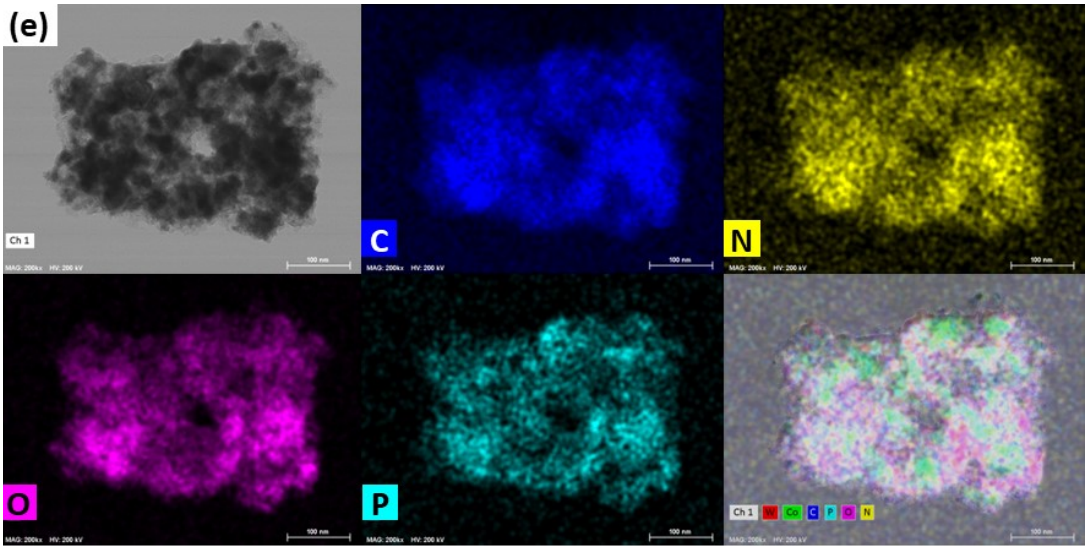
(e)
Ch 1
C
N
O
P
Ch 1

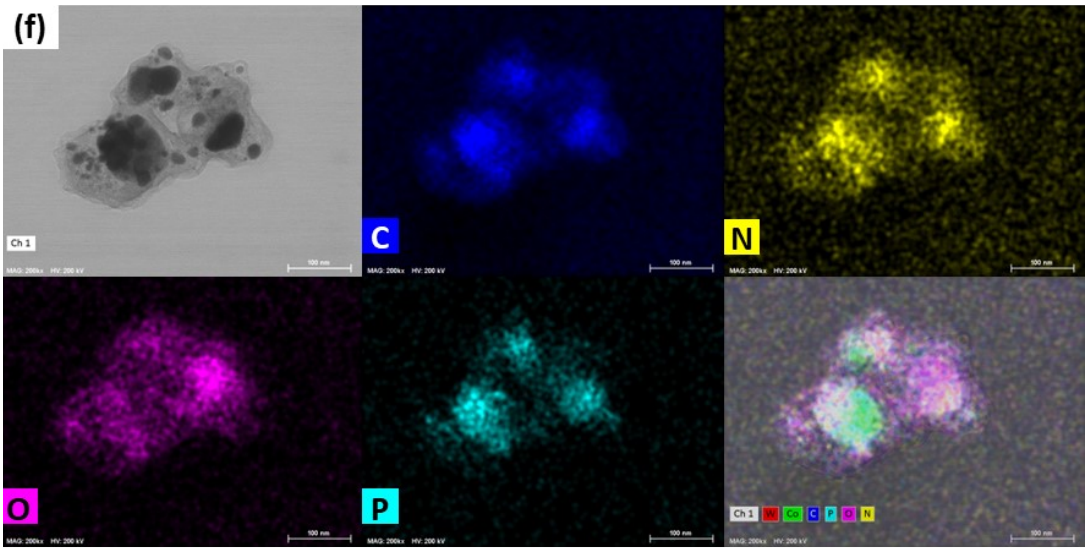
(f)
Ch 1
C
N
O
P
Ch 1

Figure S14. EDS element distribution maps (C, N, O, P, all element) for **(a)** ZIF-67, **(b)** $PW_{11}Co$@ZIF-67, **(c)** D200, **(d)** D400, **(e)** D500, **(f)** D600, and **(g)** D950. *See W and Co distribution maps in Fig. 8 in the manuscript.*

REFERENCES

1. F. Couto, A. M. V. Cavaleiro, J. D. P. de Jesus and J. E. J. Simao, *Inorganica Chimica Acta*, 1998, **281**, 225-228.
2. S. Hanelt, J. F. Friedrich, G. Orts-Gil and A. Meyer-Plath, *Carbon*, 2012, **50**, 1373-1385.
3. N. Lachman, X. Sui, T. Bendikov, H. Cohen and H. D. Wagner, *Carbon*, 2012, **50**, 1734-1739.
4. Z. Yang, Z. Yao, G. F. Li, G. Y. Fang, H. G. Nie, Z. Liu, X. M. Zhou, X. Chen and S. M. Huang, *Acs Nano*, 2012, **6**, 205-211.
5. T. F. S. Inc., XPSsimplified, https://xpssimplified.com/).
6. A. Awadallah-F, F. Hillman, S. A. Al-Muhtaseb and H. K. Jeong, *Journal of Materials Science*, 2019, **54**, 5513-5527.
7. F. Y. Tian, A. M. Cerro, A. M. Mosier, H. K. Wayment-Steele, R. S. Shine, A. Park, E. R. Webster, L. E. Johnson, M. S. Johal and L. Benz, *Journal of Physical Chemistry C*, 2014, **118**, 14449-14456.
8. S. Maldonado, S. Morin and K. J. Stevenson, *Carbon*, 2006, **44**, 1429-1437.
9. Q. P. Dai, J. F. Zhang and M. Ma, *Applied Surface Science*, 1993, **72**, 67-72.
10. B. Brena, Y. Luo, M. Nyberg, S. Carniato, K. Nilson, Y. Alfredsson, J. Ahlund, N. Martensson, H. Siegbahn and C. Puglia, *Physical Review B*, 2004, **70**.
11. D. R. Sun, L. Ye, F. X. Sun, H. Garcia and Z. H. Li, *Inorganic Chemistry*, 2017, **56**, 5203-5209.
12. M. A. Peck and M. A. Langell, *Chemistry of Materials*, 2012, **24**, 4483-4490.
13. F. Morales-Lara, M. J. Perez-Mendoza, D. Altmajer-Vaz, M. Garcia-Roman, M. Melguizo, F. Javier Lopez-Garzon and M. Domingo-Garcia, *Journal of Physical Chemistry C*, 2013, **117**, 11647-11655.
14. S. Aduru, S. Contarini and J. W. Rabalais, *Journal of Physical Chemistry*, 1986, **90**, 1683-1688.
15. K. Burger, F. Tschimarov and H. Ebel, *Journal of Electron Spectroscopy and Related Phenomena*, 1977, **10**, 461-465.
16. D. N. Hendrickson, J. M. Hollander and W. L. Jolly, *Inorganic Chemistry*, 1969, **8**, 2642-+.
17. L. L. Xiao, Q. Zhao, L. Jia, Q. Chen, J. Jiang and Q. Y. Yu, *Electrochimica Acta*, 2019, **304**, 456-464.
18. M. C. Alvarez-Galvan, G. Blanco-Brieva, M. Capel-Sanchez, S. Morales-DelaRosa, J. M. Campos-Martin and J. L. G. Fierro, *Catalysis Today*, 2018, **302**, 242-249.
19. X. N. Chen, X. H. Wang and D. Fang, *Fullerenes Nanotubes and Carbon Nanostructures*, 2020, **28**, 1048-1058.
20. W. Grunert, E. S. Shpiro, R. Feldhaus, K. Anders, G. V. Antoshin and K. M. Minachev, *Journal of Catalysis*, 1987, **107**, 522-534.
21. M. Ayiania, M. Smith, A. J. R. Hensley, L. Scudiero, J. S. McEwen and M. Garcia-Perez, *Carbon*, 2020, **162**, 528-544.
22. I. Takano, S. Isobe, T. A. Sasaki and Y. Baba, *Applied Surface Science*, 1989, **37**, 25-32.